THE INVESTIGATION OF Cr^{3+}-ACTIVATED GALLATE-BASED NEAR-INFRARED LONG-PERSISTENT PHOSPHORS

by

YI-YING LU

(Under the Direction of Zhengwei Pan)

ABSTRACT

Near infrared (NIR) long-persistent phosphors have gained considerable attention in recent years due to their potential applications in security and defense, solar energy utilization, and *in vivo* deep-tissue bio-imaging. The present work aims to discover and develop two novel series of chromium ion (Cr^{3+})-activated, gallate-based NIR persistent phosphors: Cr^{3+}-doped β-Ga_2O_3 nanowires and Cr^{3+}-doped zinc gallogermanate powders and ceramics.

The Cr^{3+}-doped β-Ga_2O_3 nanowires were synthesized by hydrothermal reaction followed by calcination. After exposed to 250–370 nm UV light for several minutes, β-Ga_2O_3:Cr^{3+} nanowires exhibit persistent luminescence in the 650–850 nm wavelength range with an afterglow time of more than 4 h. No persistent NIR luminescence was observed in nanowires before.

The Cr^{3+}-doped zinc gallogermanates were prepared by a solid-state reaction method with general chemical formula of $Zn_xGa_yGe_zO_{(x+(3y/2)+2z)}$: tCr^{3+}, mR, where R is a co-dopant selected from a group consisting of alkaline earth ions, rare earth ions, and Li^+ ions; x, y, and z are integers from 1 to 5; t is 0.01 mol% to 2 mol% based on the total moles of Ga; and m is 0 to 2 mol% based on the total moles of Ga. Any combinations of these variables can always produce materials with remarkable NIR persistent luminescence. In this dissertation, we used $Zn_3Ga_2Ge_4O_{14}$:0.1%Cr^{3+} as an example to demonstrate the superb capabilities of Cr^{3+}-doped zinc gallogermanates in excitation energy absorption, storage, NIR light conversion, and NIR light persistent luminescence.

The NIR persistent luminescence in Cr^{3+}-doped zinc gallogermanates can be effectively activated by both UV light and solar radiation. Remarkably, the materials can be quickly and repeatedly charged by solar radiation in any weather conditions, at any moment between sunrise and sunset, at any outdoor locations, and in various aqueous solutions. Seconds to minutes of solar radiation activation can result in days to weeks (> 400 h) of NIR persistent luminescence. The 400 h of persistence time is about two orders of magnitude longer than that achieved previously by others.

The afterglow mechanisms of both β-Ga_2O_3:Cr^{3+} nanowires and Cr^{3+}-doped zinc gallogermanates were studied based on the results of afterglow decay curves and thermoluminescence measurements and related models were proposed.

INDEX WORDS: Near infrared, NIR, Persistent phosphors, Persistent luminescence, Afterglow, Cr^{3+} ions, β-Ga_2O_3:Cr^{3+} nanowires, Zinc gallogermanates, $Zn_3Ga_2Ge_4O_{14}$:Cr^{3+}, NIR persistent luminescent paint, Solar radiation

THE INVESTIGATION OF Cr^{3+}-ACTIVATED GALLATE-BASED NEAR-INFRARED LONG-PERSISTENT PHOSPHORS

by

YI-YING LU

B.S., National Chung Hsing University, Taiwan, 2003

A Dissertation Submitted to the Graduate Faculty of the University of Georgia in Partial Fulfillment of the Requirements for the Degree

Doctor OF Philosophy

ATHENS, GEORGIA

2010

THE INVESTIGATION OF Cr^{3+}-ACTIVATED GALLATE-BASED NEAR-INFRARED LONG-PERSISTENT PHOSPHORS

by

YI-YING LU

Major Professor:	Zhengwei Pan
Committee:	William M. Dennis Yiping Zhao

Electronic Version Approved:

Maureen Grasso
Dean of the Graduate School
The University of Georgia
December 2010

ACKNOWLEDGEMENTS

I would like to express my deepest gratitude to my advisor Dr. Zhengwei Pan for his patience and advice in directing and implementing the research. I would also like to thank Dr. William M. Dennis and Dr. Yiping Zhao for serving on my committee. Special thanks go to Dr. Richard S. Meltzer for his valuable advice in science discussion and assistance with experiments.

I would like to thank the members of the Dr. Pan group, Wuzhao Yan, Yen-Jun Chuang and especially Dr. Feng Liu and Dr. Zhanjun Gu, for their guidance and assistance. Grateful acknowledgment goes to Dr. Feng Liu for spending his precious time on proofreading my dissertation.

I would also like to thank Shijun Lei, Judy Wu and Debra Huang for their kindness and support.

Finally, I would like to thank my family for their unconditional support and encouragement.

TABLE OF CONTENTS

Page

CHAPTER

LIST OF TABLES

Page

LIST OF FIGURES

Page

CHAPTER 1

INTRODUCTION

1.1 Long-persistent luminescence phenomenon

Long-persistent luminescence, also known as afterglow, is the phenomenon that materials can continue to emit light after removal of the irradiation source (e.g., ultraviolet light, X-ray, gamma radiation or visible natural light). The persistent luminescence usually can last for an appreciable time from seconds to hours. For the occurrence of long-persistent luminescence, two kinds of active centers are involved: emitters and traps. Emitters are centers capable of emitting radiation after they are excited. Traps do not emit radiation; however, they store excitation energy in the form of trapping electrons and holes and then release it gradually to the emitters. The exhaustive processes leading to afterglow are not clear. However, it is generally accepted that the long-persistent luminescence concerns the release of electrons from various traps in the lattices and subsequent radiative recombination with trapped holes at the emitting centers.

1.2 History of long-persistent phosphors

The discovery of long-persistent luminescence can be traced back to the 11th century in China and Japan and in the 16th century in Europe[1]. The first well-documented report of persistent luminescence dates back to the 17th century. In 1602, shoemaker and alchemist Vincenzo Casciarolo discovered strong luminescence from the mineral barite, $BaSO_4$ (Bologna stone)[2]. The first generation of green long-persistent phosphor, ZnS:Cu, was synthesized by Sidot in 1866 and has been used for practical purposes (e.g., glow-in-the-dark toys, watch dials and luminous paints) for a very long time due to its relatively high luminous efficiency[3]. For many decades, ZnS:Cu was the most widely used persistent phosphor. However it is extremely sensitive to moisture, and the duration of the afterglow is only a few hours at the most, hampering its further practical applications. People have tried to modify its long-persistent luminescence properties by substituting Cd for Zn or introducing some radioactive elements such as ^{3}H and ^{147}Pm in to the phosphors, however, the brightness and duration time are still not acceptable. Moreover, such radioactive elements are harmful to human bodies.

Before the 1990s, the main trends of luminescent subjects were lighting, laser and scintillator material applications. Afterglow was usually considered as an undesired phenomenon. Therefore, instead of exploring the way to increase the persistent time of phosphors, significant effort was directed to eliminate this phenomenon. Very little research was done on the afterglow phenomena.

1.3 Current situation and development of long-persistent phosphors

In 1996, Matsuzawa *et al*. reported a novel green long-persistent phosphor, $SrAl_2O_4:Eu^{2+}$, Dy^{3+} with a persistence time of up to 20 hours, opening the new era for the field of persistent phosphors[4]. The brightness of $SrAl_2O_4:Eu^{2+},Dy^{3+}$ is more than 10 times brighter than ZnS:Cu,Co. Moreover, the afterglow of $SrAl_2O_4:Eu^{2+},Dy^{3+}$can be activated by natural sun light. After this remarkable breakthrough, extensive research was triggered not only in the exploration of new compounds but also in deciphering the underlying mechanisms. Currently, the $SrAl_2O_4:Eu^{2+},Dy^{3+}$ and many other Eu^{2+}-activated persistent phosphors are being used as night vision materials in many important fields.

The persistent time for visible long-persistent phosphors is defined as the length of time until the afterglow intensity decays to an intensity of 0.32 mcd/m^{2}, which is about 100 times of the perception limit of the human eye[1]**. Table 1.1** lists the visible long-persistent phosphors developed by far with a persistence time of at least one hour.

The emission colors of the long-persistent phosphors developed by far are mainly in the visible regions and only blue and green long-persistent phosphors meet the requirements for high initial intensity and a sufficiently long duration time of afterglow. From **Table 1.1**, it can be seen that Eu^{2+} is the most frequently adopted activation luminescent ion in the visible long-persistent phosphors. The Eu^{2+}-activated phosphors typically exhibit broadband emission, which is generally attributed to parity allowed *d-f* transition. The emission wavelengths of Eu^{2+} in phosphors change from UV to red depending on the host lattices. The reported longest emission wavelengths is 620 nm in $Ca_2Si_5N_8{:}Eu^{2+},R^{+}$ phosphor (R = rare earth ions). The progress on red persistent phosphors is rather slow. This drought could be due to the following reasons. First, due to the lack of long-persistent luminescence mechanisms, the search of new long-persistent materials is mainly based on a laborious trial and error method. Second, the low sensitivity to red emission of the human eye, the so-called Purkinje effect, makes it more challenging to search for highly efficient red long-persistent phosphors[5]. Up until now, a well-performing red long-persistent phosphor is rare.

1.4 Motivations

For each possible application, there is a different requirement for emission wavelengths. Recently, great attention has been given to those phosphors, scintillators, and dyes whose emission wavelengths in the near-infrared (NIR; 700-2500 nm) spectral region. NIR radiation is non noninvasive as well as non-ionizing and has more effective blood and tissue penetration than UV and visible light[6]. Chermont *et al.* used NIR long-persistent luminescent nano-particles as fluorescent probes for *in vivo* bio-imaging[48]. In their experiments, the nanoparticles were excited by UV light before injection. The persistent luminescence of the particles after injection makes external illumination unnecessary, which prevents tissue autofluorescence caused by the

Table. 1.1 Visible long-persistent phosphors sorted by emission colors

Emission color	Host compound	Emitter	Co-dopant	Reference
Indigo	$Ca_{12}Al_{14}O_{33}$	Eu^{2+}	Nd^{3+}	7
Purple	$CaAl_2O_4$	Ce^{3+}		8
Blue	$CaAl_2O_4$	Eu^{2+}	Nd^{3+}	9
Blue	$Sr_4Al_{14}O_{25}$	Eu^{2+}	Dy^{3+}	10
Blue	$SrAl_4O_7$	Eu^{2+}	Dy^{3+}	11
Blue	$BaAl_2O_4$	Ce^{3+}	Dy^{3+}	12
Blue	$CaYAl_3O_7$	Ce^{3+}		13
Blue	$CaMgSi_2O_6$	Eu^{2+}	Dy^{3+}	14
Blue	$Sr_2ZnSi_2O_7$	Eu^{2+}	Dy^{3+}	15
Blue	$M_3MgSi_2O_8$ (M=Ca,Sr,Ba)	Eu^{2+}	Dy^{3+}	16
Blue	$Ca_2Al_2SiO_7$	Eu^{2+}	Dy^{3+}	17
Blue	$CaAl_2Si_2O_8$	Eu^{2+}	Dy^{3+}	18
Blue	CaS	Bi^{3+}	Tm^{3+}	19
Blue	$Ca_2P_2O_7$	Eu^{2+}	Y^{3+}	20
Blue	$Sr_2P_2O_7$	Eu^{2+}	Y^{3+}	21
Blue	$SrMg_2P_2O_8$	Eu^{2+}	Ce^{3+}	22
Blue to Green	$M_2MgSi_2O_7$ (M=Ca,Sr,Ba)	Eu^{2+}	Dy^{3+}	23
Green	$SrAl_2O_4$	Eu^{2+}	Dy^{3+}	4
Green	$BaAl_2O_4$	Eu^{2+}	Dy^{3+}	24
Green	$MgAl_2O_4$	Ce^{3+}		25
Green	$CaAl_2O_4$	Tb^{3+}		26
Green	$CaAl_2O_4$	Tb^{3+}	Ce^{3+}	27
Green	$MgAl_2O_4$	Tb^{3+}		28
Green	$Sr_2Al_2SiO_7$	Eu^{2+}	Dy^{3+}	17
Green	$(Zn,Mg)Ga_2O_4$	Mn^{2+}		29
Green	Lu_2O_3	Tb^{3+}	Ca^{2+}, Sr^{2+} or Ba^{2+}	30
Green	ZnS	Cu^{+}	Co^{2+}	31
Yellow	$Ca_2Al_2SiO_7$	Mn^{2+}	Ce^{3+}	32
Yellow	$CaGa_2S_4$	Eu^{2+}	Ho^{3+}	33
Yellow to Orange	Y_2O_2S	Tm^{3+}		34
Orange	$Ca_2Si_5N_8$	Eu^{2+}	Tm^{3+}	35
Orange	$CdSiO_3$	Mn^{2+}		36
Orange to Red	MO(M=Ca,Sr,Ba)	Eu^{3+}		37
Orange to Red	Y_2O_2S	Ti^{4+}	Eu^{3+}, Mg^{2+}	38
Orange to Red	Y_2O_2S	Sm^{3+}		39
Orange to Red	SrS	Eu^{2+}	Dy^{3+}	40
Red	$MgGeO_3$	Mn^{2+}	Yb^{3+}	41
Red	Y_2O_3	Eu^{3+}	Ti^{4+}, Mg^{2+}	42
Red	Gd_2O_2S	Eu^{3+}	Ti^{4+}, Mg^{2+}	43
Red	CaS	Eu^{2+}	Tm^{3+}	44
Red	$Zn_3(PO_4)_2$	Mn^{2+}	Ga^{3+}	45
Red	$CaTiO_3$	Pr^{3+}		46
Red	$Ca_2Zn_4Ti_{16}O_{38}$	Pr^{3+}		47
Red	$MgSiO_3$	Mn^{2+}	Eu^{2+}, Dy^{3+}	32

continuous external illumination and thus increases the signal/noise ratio. Moreover, NIR wavelengths are suitable for night surveillance[49] as they are invisible to the human eye and can only be detected by night-vision devices.

However, the progress on NIR long-persistent phosphors is too slow to fulfill the increasing demands on bio-imaging, labeling and homeland security. Up until now, only a few NIR persistent phosphors were reported, which were by introducing suitable donor-acceptor pairs (e.g., Eu^{2+}-Mn^{2+}, Eu^{2+}-Er^{3+}) into the host[48,50]. In these phosphors, the luminescence center of a known long-persistent phosphor is used as the donor, and another ion, which can emit the desired color, is chosen as the acceptor. **Table 1.2** lists the NIR long-persistent phosphors developed so far. The limited energy transfer efficiency and the inevitable visible emission from the donor ions (e.g., green emission from Eu^{2+}), however, hinder the further investigations of these phosphors[51].

The work presented in this dissertation aims to discover and synthesize novel long-persistent phosphors in the NIR region. For this purpose, suitable emitters whose emission in the NIR region and proper hosts that can enhance the NIR emission are necessary. Up until now, rare earth and transition metal ions are the two major groups widely used as the luminescent centers. Taking pure NIR persistent emission into consideration, among the rare earth ions the potential candidates for the luminescent centers could be narrowed to Eu^{2+} ions. For most other rare earth ions, either the 5*d* level are too high to be charged or there accompanies of inevitable visible 4*f*-4*f* transition[52]. Moreover, finding an appropriate host that can lower the emitting level of Eu^{2+} ions to produce NIR emission is another challenge[2].

Among the transition metal ions activated phosphors, chromium ion in the trivalent states, Cr^{3+}, is a favorable luminescent center because of its narrow R-line emission at around

Table. 1.2 Near-infrared long persistent phosphors

Emission wavelength (nm)	Host compound	Emitter	Co-dopant	Reference
520 and 1530	$SrAl_2O_4$	Er^{3+}	Eu^{2+}, Dy^{3+}	50
520 and 800	$Ca_{0.2}Zn_{0.9}Mg_{0.9}Si_2O_6$	Mn^{2+}	Eu^{2+}, Dy^{3+}	48
660-1300	$La_3Ga_5GeO_{14}$	Cr^{3+}	Zn^{2+}, Li^{+}, Pb^{2+}, Zn^{2+}, Eu^{3+}, Tm^{3+}, Dy^{3+}	51,52

696 nm due to the spin forbidden $^2E \rightarrow ^4A_2$ transition, or a broadband emission covering 650-1200 nm due to the spin allowed $^4T_2 \rightarrow ^4A_2$ transition, which strongly depends on the crystalline field strength of the hosts[53].

In the development of Cr^{3+}-activated NIR phosphors, gallates, such as $Ln_3Ga_5O_{12}:Cr^{3+}$ (Ln = Y, Gd, La or Lu)[54], $LiGa_5O_8:Cr^{3+}$ [55], $M_3Ga_2Ge_4O_{14}:Cr^{3+}$ (M = Sr or Ca)[56], and $La_3Ga_5GeO_{14}:Cr^{3+}$[57], were frequently used as the hosts because of the excellent ability of Cr^{3+} ions to substitute for Ga^{3+} ions in distorted octahedral sites and the suitable host crystal field strength around Cr^{3+} ions for achieving intense NIR luminescence[58]. Inspired by the success of the Cr^{3+}-activated gallate NIR laser crystals, persistent NIR luminescence with persistence time of more than 1 h was recently realized in Cr^{3+}-doped lanthanide gallogermanate ($La_3Ga_5GeO_{14}:Cr^{3+}$) phosphors by our group[51] and Jia *et al*[52]. For practical applications, however, the persistence time needs to be significantly increased, at least reaches the level of the commercial green and blue persistent phosphors.

In traditional definition, the persistence time of visible long-persistent phosphors is defined according to eye sensitivity. However, for the long-persistent phosphors with emission wavelengths in the NIR region, the definition is no longer valid, because the infrared signal is invisible to the human eye. The persistence time for infrared long-persistent phosphors should then be determined by the sensitivity of the detection systems such as night vision goggles, infrared cameras, or infrared detectors.

1.5 Organization of the dissertation

In this dissertation, we have discovered and synthesized two novel series of Cr^{3+}-doped gallate-based NIR long-persistent phosphors: β-Ga_2O_3:Cr^{3+} nanowires and Cr^{3+}-doped zinc gallogermanates. Chapter 2 gives an introduction on the optical properties of the Cr^{3+}-activated NIR long-persistent phosphors. In Chapter 3, we present NIR long-persistent luminescence from β-Ga_2O_3:Cr^{3+} nanowires prepared by hydrothermal method followed by calcinations at high temperature. The emission wavelengths and origin of the NIR persistent luminescence are studied by measuring the afterglow spectrum. The optimal activation wavelengths that can induce NIR long-persistent luminescence are determined. Chapter 4 presents a novel series of super-long lasting NIR persistent phosphors, Cr^{3+}-doped zinc gallogermanates, which have persistent time of up to 400 h. The performance of the Cr^{3+}-doped zinc gallogermanates were measured under the activation of various irradiation sources, including UV light, natural solar radiation, and fluorescent lamp light. The possible persistent luminescence mechanism was proposed basing on the results obtain from afterglow decay measurements. Finally, the conclusions and outlook were given in Chapter 5.

CHAPTER 2

PRELIMINARY UNDERSTANDING OF Cr^{3+}-ACTIVATED LONG-PERSISTENT PHOSPHORS

2.1 Introduction

Cr^{3+} ions have been adopted as luminescent centers for various phosphors. Most of the previous studies focused on in the fabrication of NIR laser crytals[54]. Until very recently, Cr^{3+} ions were used as the emitting center in NIR persistent phosphors. In this chapter, we give a brief introduction on the optical properties of Cr^{3+} ions which is useful for better understanding the content in Chapter 3 and Chapter 4.

2.2 Photoluminescence of Cr^{3+} ions in phosphors

2.2.1 Definition of photoluminescence

Photoluminescence is a process in which materials absorb photons (electromagnetic radiation) results in an excitation to a higher energy state, and then release that energy in the form of light. Photoluminescence can be further divided in two major types: intrinsic and extrinsic luminescence. In the case of intrinsic luminescence, includes band-to-band luminescence, exciton luminescence and cross-luminescence. Extrinsic luminescence is usually caused by the impurities. In this dissertation, we focus only on the extrinsic luminescence in phosphors. When foreign atoms are introduced into a host, the optical properties of these materials will be conferred. This is because impurities will create localized energy levels in the forbidden band of the host, which allow them to give rise to the appearance of optical transitions whose energy is lower than the band gap of the host. Due to these energy levels that are not present in the hosts, various emission wavelengths corresponding to transitions from various levels will occur. Therefore, doping is the strategy to engineer the optical properties of semiconductors or insulators. Rare earth and transition metal ions are the two types of widely used dopants.

2.2.2 Crystal field theory on transition metal ions

The interest in transition metal ions arises from their wide applications in commercial phosphors and tunable solid state lasers[1]. Transition metal ions are found in the fourth period of the periodic table, from scandium (element 21) with electronic configuration [**Ar**]$3d^{1}4s^{2}$ to zinc (element 30) with electronic configuration [**Ar**]$3d^{10}4s^{2}$. In order to form stable ions, transition meal ions have a tendency to lose the outer $4s$ electrons and possible some $3d$ electrons[59]. The $3d$ orbitals lie on the outer shells of transition metal ions and they interact strongly with the host crystal. Therefore, to determine the energy levels of transition metal ions in a crystal, one should also consider the interaction between the neighboring ions and the $3d$ electrons of transition metal ions.

The energy states of the impurity ion in a crystal can be determined by solving a many-body Schrödinger equation. However, the tremendous amount of particles comprising the material makes it impossible to compute directly. One approximate approach to this problem is the crystal field theory. Crystal field theory assumes that the ligands are point charges which create the crystal field. This theory ignores all the covalent bonding and does not take account of the overlap of orbitals[59].

Crystal field theory shows that the splitting of $3d$ energy level depends strongly on the symmetry of the crystallographic site. In the free ion case, the *d*-orbitals are energetically degenerate, but their energies become differentiated and raised with the approach of the ligands. When the transition metal ions are in the sites with octahedral symmetry, the original degeneracy is destroyed, and the energies are split into two groups: d_{z^2} and $d_{x^2-y^2}$ orbitals (called e_g) and d_{xy}, d_{xz}, and d_{yz} orbitals (called t_{2g}). The d_{z^2} and $d_{x^2-y^2}$ orbitals point towards the ligand ions while the d_{xy}, d_{xz} and d_{yz} orbitals lie between ligand ions (**Figure 2.1**). Therefore, an electron placed in the d_{xy}, d_{xz}, and d_{yz} orbitals suffer less repulsion than one placed in the d_{z^2} and $d_{x^2-y^2}$ orbitals. This result suggests that the e_g energy level goes higher than the t_{2g} energy level, as shown in **Figure 2.1**. The energy difference between these two groups of orbitals is given as the symbol Δ.

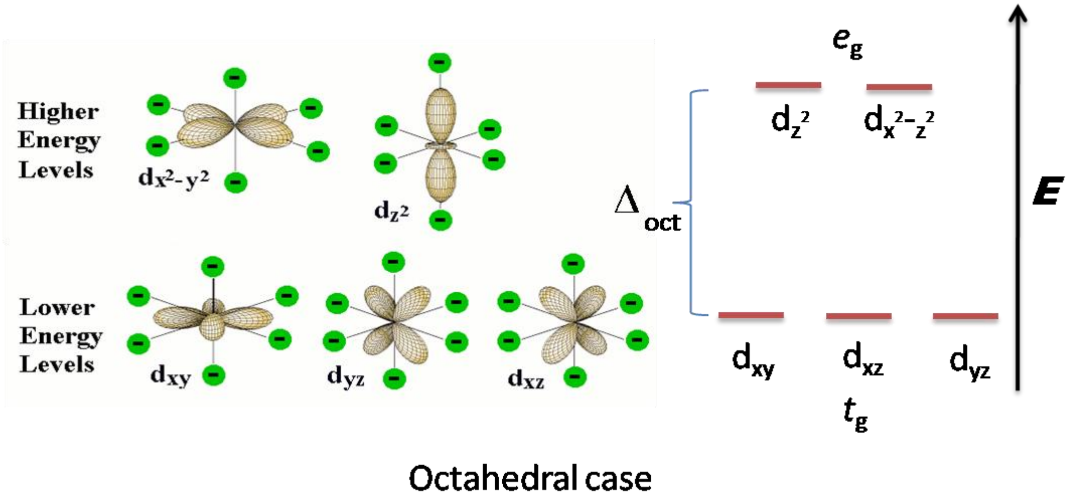

Figure 2.1 Representations and energy level splitting of *d*-orbitals in octahedral symmetry. The green circles are the coordinating electron-pairs of the ligands.

2.2.3 Tanabe-Sugano diagram of Cr^{3+} ions

Before Tanabe and Sugano published their paper on the absorption spectra of complex ions[60-62], little was known about the excited states of transition metal ions. They used crystal field theory and Racah parameters to explain the absorption spectra of transition metal ions in octahedral field.

The Tanabe-Sugano diagram shows the relative positions of energy levels arising from the splitting of the degenerate free-ion states of transition metals as the function of the crystal field strength. Among the transition ions, Cr^{3+} ion is the popular luminescent center in many phosphors. The Tanabe-Sugano diagram of $3d^3$ ions in octahedral fields is shown in **Figure 2.2**. In this figure, Dq represents the interaction of the *d* electrons with the electrostatic fields of the ligands (crystal field), and B is Racah parameter. The left-hand side of the diagram corresponds to the free ion case (Dq = 0), and the split components resulting from the crystal-field are shown on the right side. The term symbols for free-ion states of transition metal ion are labeled as ^{2S+1}L, where S is the total spin quantum number and L is the total orbital angular momentum. The degeneracy of these levels is 2L+1 and can be removed by the crystal field. Crystal field energy levels are labeled as ^{2S+1}X, where X can be A for orbital singlet, E for a doublet and T for a triplet. The ground state of a free ion of d^3 configuration is ^4F, and the ^4F state is further split into a $^4A_{2g}$ ground state and two excited states: $^4T_{2g}$ and $^4T_{1g}$**,** which are classified by irreducible representations of the O_h group. The subscript g means the wavefunctions are even under inversion through the centre of symmetry possessed by the octahedron. Similarly, each of the degenerate excited states of the free ion is split into different A, T and E levels. And, these irreducible representations can be further split into their respective multiples by the weak spin-orbit interaction (e.g., doublet energy level ^2E_g: $R_1$and R_2 lines of $Al_2O_3:Cr^{3+}$).

The diagram shown in **Figure 2.2** gives the trend of the excited states energy level relative to the ground state of Cr^{3+} with the variation of the octahedral crystal field. The inset in **Figure 2.2** shows the electronic configuration of the irreducible representations. We can see that some excited states are almost independent of the crystal field (e.g., ^2E_g). This is because the $^4A_{2g}$ ground state and the ^2E_g level belong to the same t^3 electronic configuration. On the other hand, $^4T_{2g}$ level belongs to different electronic configuration t^2e, where the *e* orbital points along the axes of the octahedron directly towards the ligands. Therefore, the $^4T_{2g}$ level is sensitive to the variation of Dq.

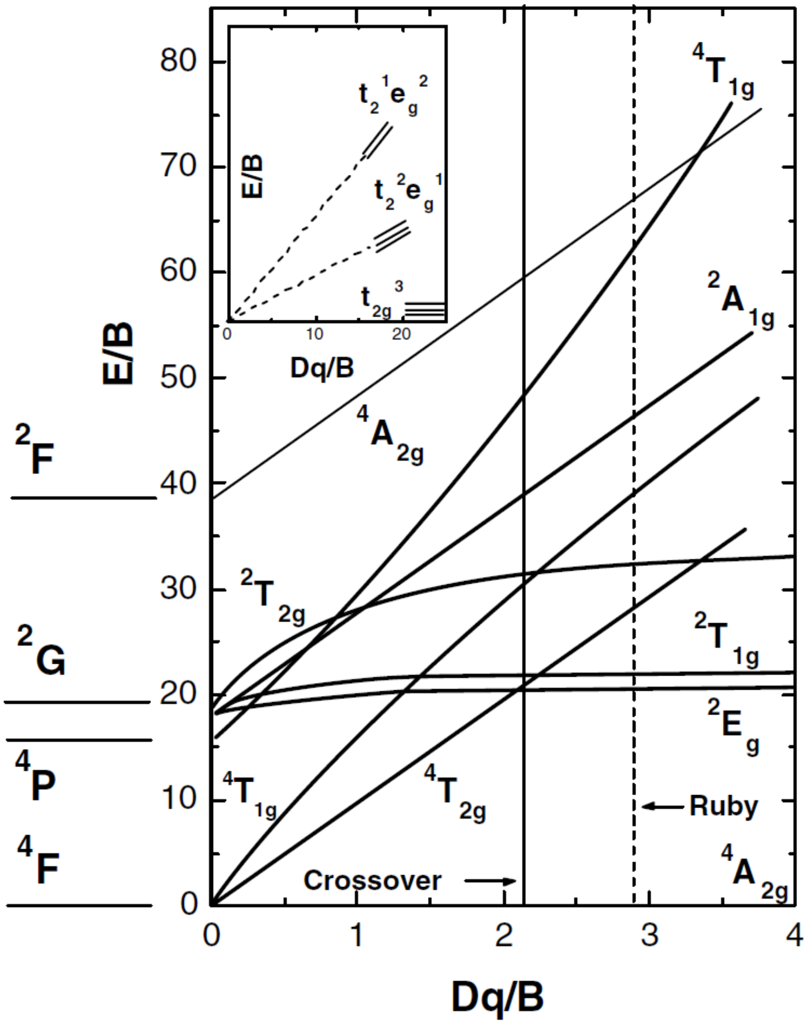

Figure 2.2 Tanabe-Sugano diagram of 3d^3 ion in octahedral field[59].

In octahedral field, the ground state of Cr^{3+} ion is always the orbital singlet $^4A_{2g,}$ and the first excited state is determined by the crystal field. When the crystal field is strong (Dq/B >2.3), the first excited state will be the ^2E_g term which gives a narrow sharp luminescence band, like the case in Al_2O_3:Cr^{3+} (ruby). In weak crystal field (Dq/B<2.3), the $^4T_{2g}$ term will become the lowest excited state which gives a broadband emission from 650-1200 nm, like the case in $ZnWO_4$:Cr^{3+}. For intermediate crystal field (Dq/B~2.3), the splitting energy ΔE between $^4T_{2g}$ and ^2E_g, is small and can be bridged by the phonon at room temperature leading the coexistence of the broadband $^4T_{2g} \rightarrow ^4A_{2g}$ and the sharp $^2E_g \rightarrow ^4A_{2g}$ emissions. Since the $^2E_g \rightarrow ^4A_{2g}$ transition is spin-forbidden transition, the lifetime is of the order of milliseconds. On the other hand, the lifetime of the broadband emission which is spin-allowed and is around microseconds. The Cr^{3+} emission can change from a sharp line to a broadband, depending on the crystal field strength. For this reason, the different emissions of Cr^{3+} ions can partly reflect the crystal structure of the host.

2.3 Long-persistent luminescence mechanisms

2.3.1 Traps for long-persistent luminescence

As mentioned in Chapter 1, for the occurrence of long-persistent luminescence, traps are necessary because they can capture charge carriers before their recombination at emission centers for an appropriate period. These trapping states are usually associated with defects such as interstitials, vacancies, or impurities. This is because defects in the crystal structure will generate metastable energy levels in the forbidden band. The metastable energy levels can be a trap or a recombination center depending on their locations in the forbidden band, as shown in **Figures 2.3**. The energy level located close to conduction band is a potential electron trap. On the other hand, the one located close to valence band is a potential hole trap[1].

The energy difference between the trap level and the conduction band bottom for a electron trap, or that between the valence top and the trap level for a hole trap is called activation energy or trap depth. Trap depth plays a key role in determining the duration time of afterglow. If the trap depth is too deep, the trapped charge carriers can remain in the trap for a long time since they cannot acquire enough energy at room temperature and may not show long-persistent luminescence. On the other hand, if the trap depth is too shallow, traps will be evacuated too quickly at room temperature resulting in short afterglow.

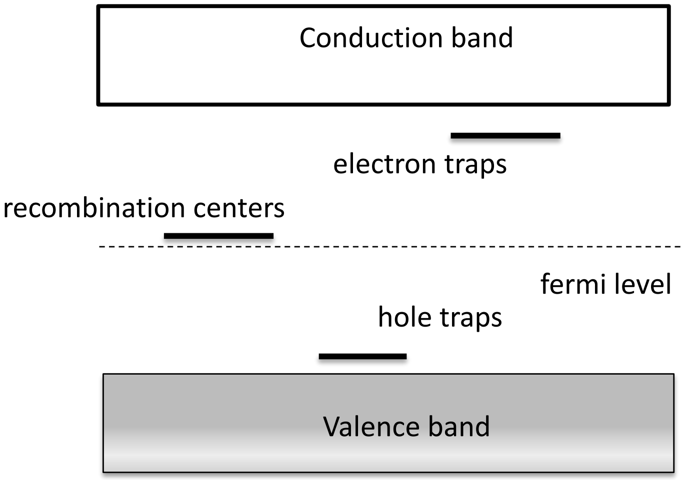

Figure 2.3 Energy level diagram of dopants in a phosphor.

The suitable trap depth for long-persistent phosphors was reported to be around 0.6 eV[4,9,63] and the thermoluminescence peak corresponding to this trap depth should locate in the range around or above room temperature[64]. The liberation of charge carriers described above is governed by thermal energy, therefore, it is temperature dependent. However, the detrapping processes can also proceed through tunneling which may be a temperature independent process or a thermal-assisted tunneling[65]. Trap density is another important factor modifying the properties of afterglow. Too many defects in the crystal may compete with recombination centers and thus may lead to nonradiative transitions.

The formation of defects depends on the growth process of the crystal or the preparation methods. During the growth of the crystal, defects are easily formed when the ionic size difference and dislocation of lattice ions occur. Therefore, introduction of foreign atoms into the crystalline structure is one main strategy to create traps. Recently, our group studied the effect of co-dopants (Li^+, Zn^{2+},Ca^{2+}, Mg^{2+}, and Dy^{3+}) on the afterglow of $La_3G_5GeO_{14}$:Cr^{3+}, and found that Zn^{2+} co-doped samples have the longest persistence time[51].

2.3.2 Long-persistent luminescence process

The popular explanation on the persistent luminescence mechanisms is based on the electron trapping and detrapping processes in phosphors[66]. The mechanism of trapping is related to electron delocalization or tunneling[8]. Before the electrons can be captured by distant traps, they must be delivered to the conduction band. Such process of delivering of an electron is associated with electron delocalization, and can be achieved by several ways, such as photon-assisted delocalization, and phonon-assisted delocalization[1]. In one photon-assisted delocalization, the excited state of the electron is overlapped with the conduction band. If the excited states are far below the conduction band, two photon or three photon processes may occur. In phonon-assisted delocalization, the excited state of the electron is just below but very close to the conduction band, and the energy difference between the excited states and conduction band can be bridged with phonon energy. Another form of electron trapping mechanism is tunneling. Tunneling is a quantum mechanical process, which is temperature independent. For the occurrence of tunneling, trap level and trapped electrons should be close enough to enable the tunneling process to take place. In this process, electrons can directly tunnel to adjacent traps and will thus not go through the conduction band.

After trapping, the trapped electrons can be liberated by several mechanisms. These include: (1) thermal (phonon)-assisted detrapping, (2) photon-assisted detrapping, (3) tunneling, and thermal-assisted tunneling[1]. In thermal-assisted detrapping, which is the major way for detrapping, the trapped electrons obtain enough energy from thermal lattice vibration. In photon-assisted detrapping, photon energy is used to evacuate the traps followed by the recombination.

Such phenomenon is also called photo-stimulated emissions. In tunneling detrapping process, trapped electrons escape by tunneling through an energy barrier. In the tunneling case, the reciprocal of the afterglow intensity will show a nearly linear dependence on the decay time.

Recently, our group proposed the persistent luminescence mechanism for $La_3G_5GeO_{14}$:Cr^{3+},Zn^{2+} phosphor under different irradiation energies[51]. Under UV irradiation, part of the excited electrons of Cr^{3+} ions are trapped by the neighboring oxygen vacancies (V_O), which are close to the bottom of the conduction band and locate in the vicinity of the photogenerated Cr^{4+} ions. These trapped electrons are then thermally released to the photogenerated Cr^{4+} ions, leading to effective Cr^{3+} afterglow emission. For the case of blue light irradiation, the energy is perhaps too low to induce the above phosphorescence process. However, the blue light energy may activate the F centers (i.e., Cr^{3+}e-) in the phosphor, which were found to exist in the lanthanum-based crystals[67]. Electrons are thermally released from the F centers to the neighbor traps at the Cr^{4+} levels, leading to persistent emission of Cr^{3+} ions.

2.4 Thermoluminescence dynamics

Thermoluminescence is defined as the thermally stimulated emission during heating from a semiconductor or an insulator following the previous absorption of energy from radiation[64]. One shouldn't be misled by the term *thermoluminescence* and consider heating is the excitation source of the luminescence. In fact, the essential excitation source for the thermoluminescence described here is the radiation which the sample is previously exposed to. Heating just triggers the liberation of the charge carriers at traps that leads to subsequent radioactive recombinations. The thermoluminescence process can be explained by a simple two-level model proposed by Jablonski (**Figure 2.4**)[68]. During irradiation, electrons are pumped from ground state (*g* level) to excited state (*e* level). In the case of photoluminescence, electrons from *e* level directly return to

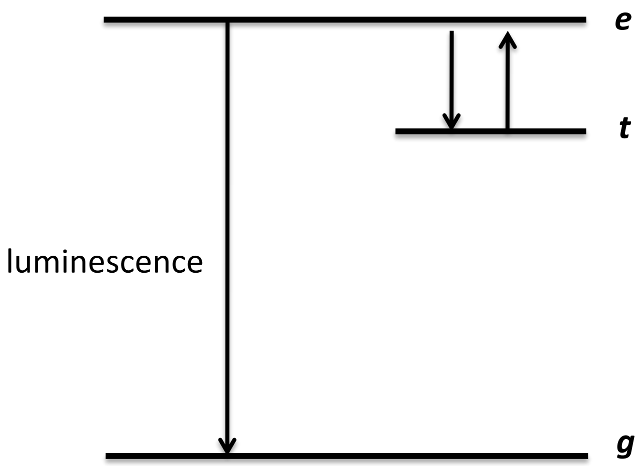

Figure 2.4 Schematic diagram of two-level system for a thermoluminescence process.

ground state *g*. However, if the electrons are captured by metastable level (*t* level), they will remain there until they acquire enough energy to escape to *e* level. Therefore, the emission is delayed and afterglow occurs.

Up to now, many efforts have been made to develop the theoretical methods to analyze the thermoluminescence. Most of these investigations were based on the pioneered papers by Randall and Wilkins[69]. This original model was based on a system consisting of one trap and one recombination center. Under irradiation, electrons are promoted from valence band to conduction band and holes are left behind in the valence band. The free electrons can be captured by the trap, while the free holes can be trapped at recombination centers. They made an assumption that once the electrons escaped from the trap level, they would return to the ground state and recombine with the holes instantaneously to emit luminescence. In this case, the mean time (τ) of a trapped charge carrier spent in the trap at temperature T depends on the trap depth E (activation energy) as well as temperature T and can be written as

$$\tau = s^{-1} e^{(E/kT)}, \tag{2.1}$$

where s is frequency factor, k is Boltzmann’s constant.

The intensity of the thermoluminescence $I(t)$ is proportional to the rate of release of electrons from the trap, and is given by

$$I(t) = n(t) s e^{-E/KT} \ , \tag{2.2}$$

where $n(t)$ is the number of trapping electrons at time t.

Note that equation (2.2) is only valid when the probability of retrapping is small and negligible.

In 1948, Garlick and Gibson[70] proposed another model and took into consideration of the effect of the retrapping. According to their model, the thermoluminescence intensity can be expressed as

$$I(t) = \frac{n(t)^2}{N} s e^{-E/KT} \ , \tag{2.3}$$

where N is the total number of traps.

May and Partridge[71] later found that not all the thermoluminescence curves can be fit well by kinetic order one or two. Therefore, they proposed that $I(t)$ should be more generally expressed in terms of n^b, where b is an empirically determined parameter and is not necessarily 1 or 2.

$$I(t) = n^b s' e^{-E/KT} \ , \tag{2.4}$$

where s' is the effective preexponential factor for general-order kinetics.

In a typical thermoluminescence experiment, the sample is heated with a linear heating rate resulting in the temperature varying as $T(t) = T_0 + \beta t$, where β is the linear heating rate (K/s). The change of $n(t)$ can be expressed as:

$$\frac{dn(T(t))}{dt} = \frac{dn(T)}{dT}\frac{dT}{dt} = \beta \frac{dn(T)}{dT} \ . \tag{2.5}$$

Therefore, equations (2.2) can be rewritten as a function of temperature T:

$$I(T) = n_0 s \exp(-\frac{E}{kT}) \exp[-\frac{s}{\beta}\int_{T0}^{T} \exp(-\frac{E}{kT'})dT'] \quad , \qquad (2.6)$$

where n_0 is the number of trapped electrons at time $t = 0$.

Similarly, the equation for Garlick and Gibson model is:

$$I(T) = n_0^2 \frac{s}{N} \exp(-\frac{E}{kT})[1 + (n_0 s / N\beta)\int_{T_0}^{T} \exp(-\frac{E}{kT'})dT']^{-2} \quad , \qquad (2.7)$$

and that for May and Partridge model is:

$$I(T) = s'' n_0 \exp(-\frac{E}{kT})[1 + (\frac{s''(b-1)}{\beta})\int_{T_0}^{T} \exp(-\frac{E}{kT'})dT']^{-\frac{b}{b-1}} \quad , \qquad (2.8)$$

where $s'' = s' n_0^{b-1}$ is an empirical parameter acting as effective frequency factor for general-order kinetics.

From equations (2.6) and (2.7), we can see that the thermoluminescence intensity in Randall and Wilkins model is proportional to n_0 and that in the Garlick and Gibson model is proportional to $n_0{}^2$. Therefore, these two equations are also called first-order and second-order kinetics respectively.

2.5 Optical measurements

2.5.1 Photoluminescence excitation and emission spectra

Excitation and emission spectra are two primary and straightforward plots that can reveal the optical properties of a material. The excitation spectrum gives the dependence of emission intensity, monitored at a fixed emission wavelength, upon scanning the excitation wavelength. A block diagram for measuring the excitation spectrum is shown schematically in **Figure 2.5**. Usually, there is one monochromator between excitation source and sample for continuously selecting desired excitation wavelengths. An appropriate cutoff filter placed between the sample and the photomultiplier tube (PMT) can pass the emission from the sample while absorb the reflected excitation radiation. The emission signal from the sample is feed into a photomultiplier tube. The signal is then amplified by an amplifier (Amp) and recorded by a computer as y axis. The excitation wavelengths selected by the monochromator is record as x axis.

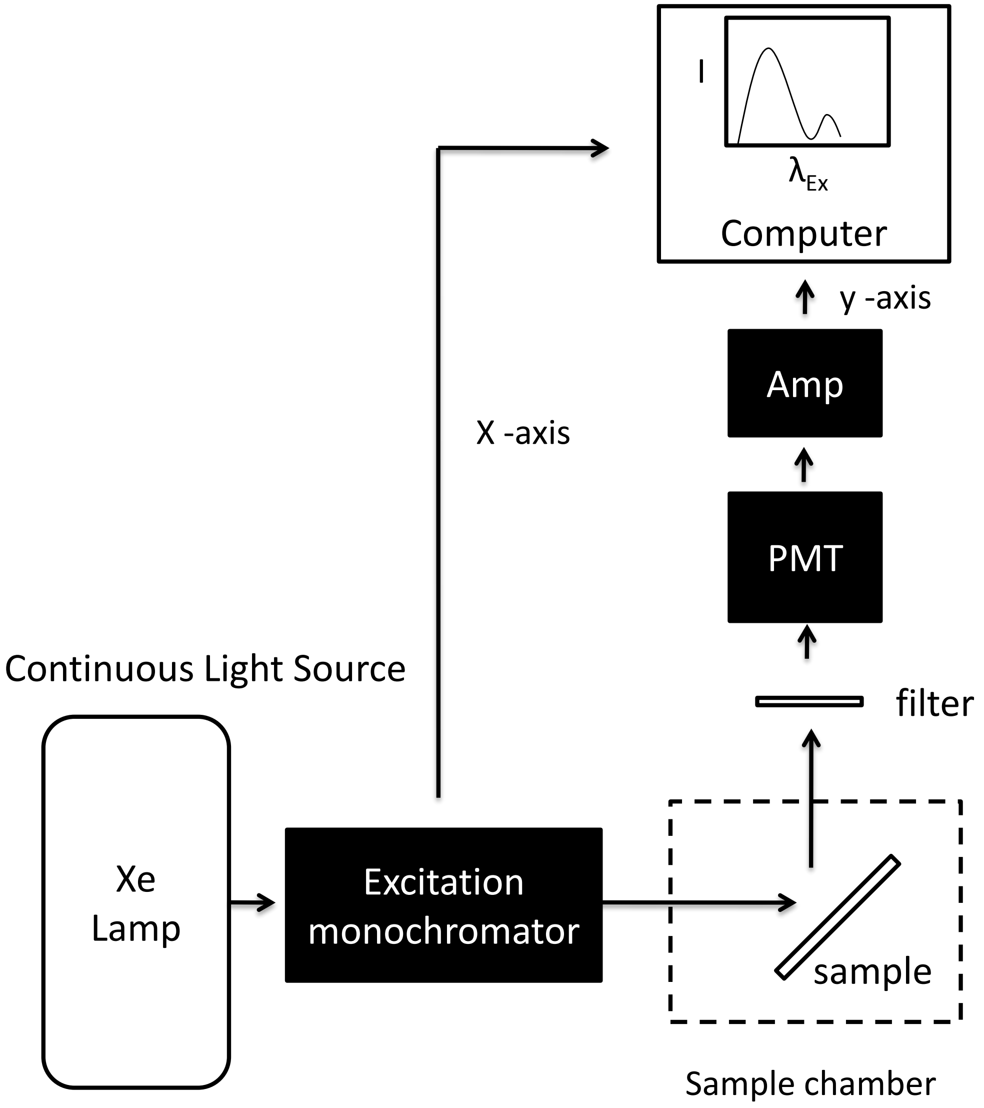

Figure 2.5 Schematic diagram a typical experimental arrangement for measuring the excitation spectrum.

The emission spectrum is the wavelength distribution of an emission measured under a fixed excitation wavelength. A block diagram for measuring the emission spectrum is shown schematically in **Figure 2.6**. To obtain the emission spectrum, the sample is excited and the emission wavelengths are scanned by emission monochromator. The appropriate cutoff filter serves the same purpose as mentioned above. In this experiment, the emission wavelengths form the sample are selected by the monochromator and recorded as x-axis.

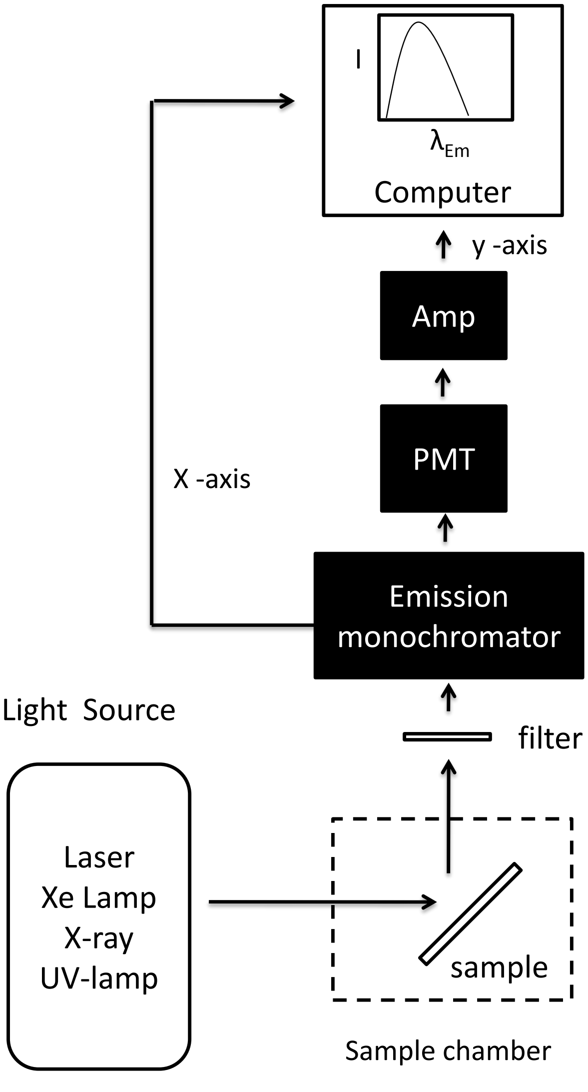

Figure 2.6 Schematic diagram of a typical experimental arrangement for measuring the emission spectrum.

The excitation and emission spectra of $La_3Ga_5GeO_{14}$:Cr^{3+} is given as an example to better illustrate the measurement (**Figure 2.7**). From **Figure 2.7**, it clearly shows that the emission occur at longer wavelengths than the excitation radiation, which means that the energy of an emitted photon is usually less than that of the photon which excited the luminescence. This phenomenon is due to the Stokes shift. Moreover, the intensity of two broad bands in excitation spectrum is not equal when monitored at the fixed emission wavelength. This result is due to the different conversation efficiency of the excitation energy into emission energy for the two absorption process that give rise to the two broad bands in the excitation spectrum.

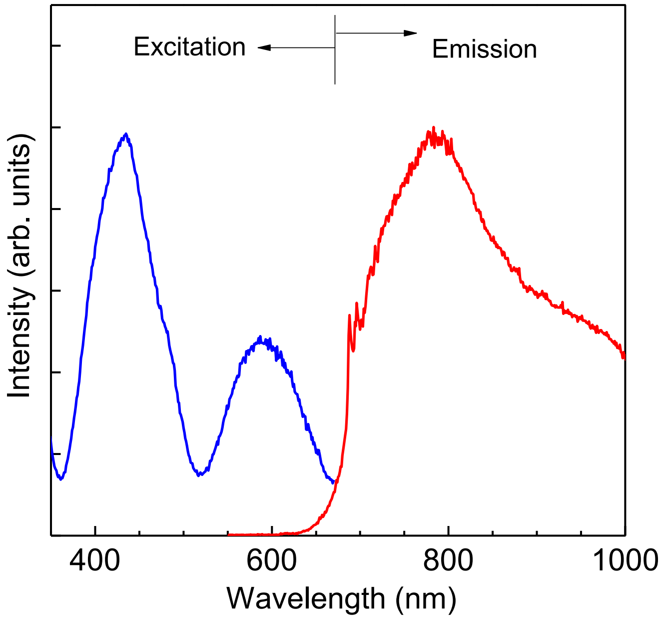

Figure 2.7 Excitation and emission spectra of $La_3Ga_5GeO_{14}$:Cr^{3+}phosphor [51].

2.5.2 Thermoluminescence measurement

Thermoluminescence measurement is a major technique for the characterizations of various types of defects in the host and has been widely used in various applications, such as meterorites study, archaeological age determination, as well as solid state defect structure analysis[64]. Thermoluminescence curves are obtained by plotting luminescence intensity as a function of sample temperature. Thermoluminescence curve consists of several peaks and some of them may overlap with each other. Each peak corresponds to different depths of traps. As a result, the relationship between the temperature and the glow intensity has been widely used to determine trapping energy and detrapping mechanisms.

A block diagram for thermoluminescence measurement is shown in **Figure 2.8**. The typical measurement system consists of a programmable temperature controller, a heater, a photomultiplier tube, and a computer. Constant heating rate is accurately maintained by the programmable temperature controller and is recorded as x-axis. The luminescence from the

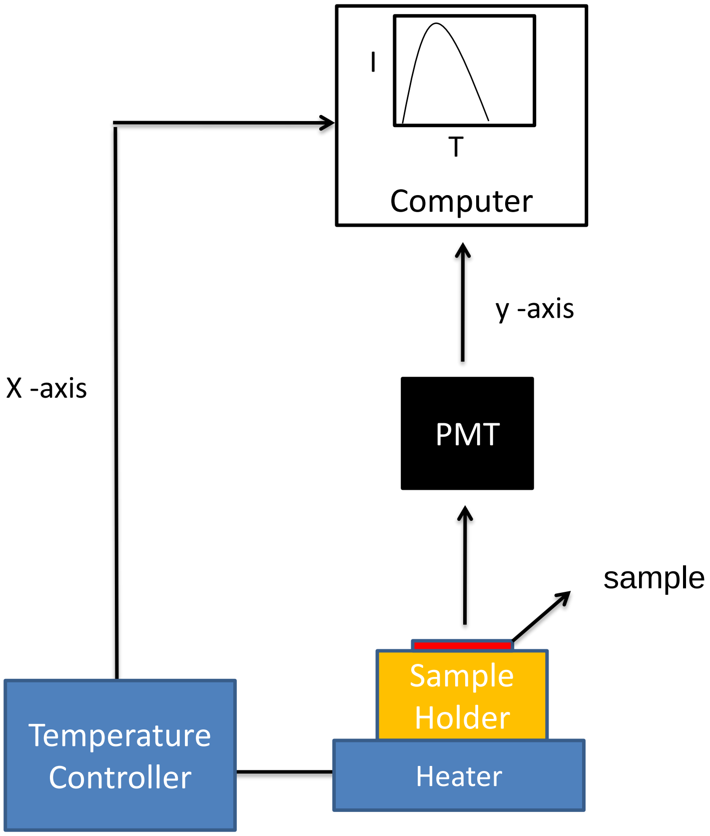

Figure 2.8 Schematic diagram of a typical experimental arrangement for measuring the thermoluminescence curves.

sample is detected by the photomultiplier tube and recorded as y axis. **Figure 2.9a** and **2.9b** show the first-order and second-order kinetic thermoluminescence curves calculated by using equations (2.6) and (2.7). The parameters are E = 1.5 eV, $s = 10^{12}$ s^{-1}, n_0 = N= 10^3 m^{-3}. It can be seen that the thermoluminescence peak of the first order kinetic is asymmetric whereas the second order kinetic is more symmetric. This is because that in the second order kinetic case, the emission is delayed by the retrapping and thus more thermoluminescence can occur at the higher temperature range.

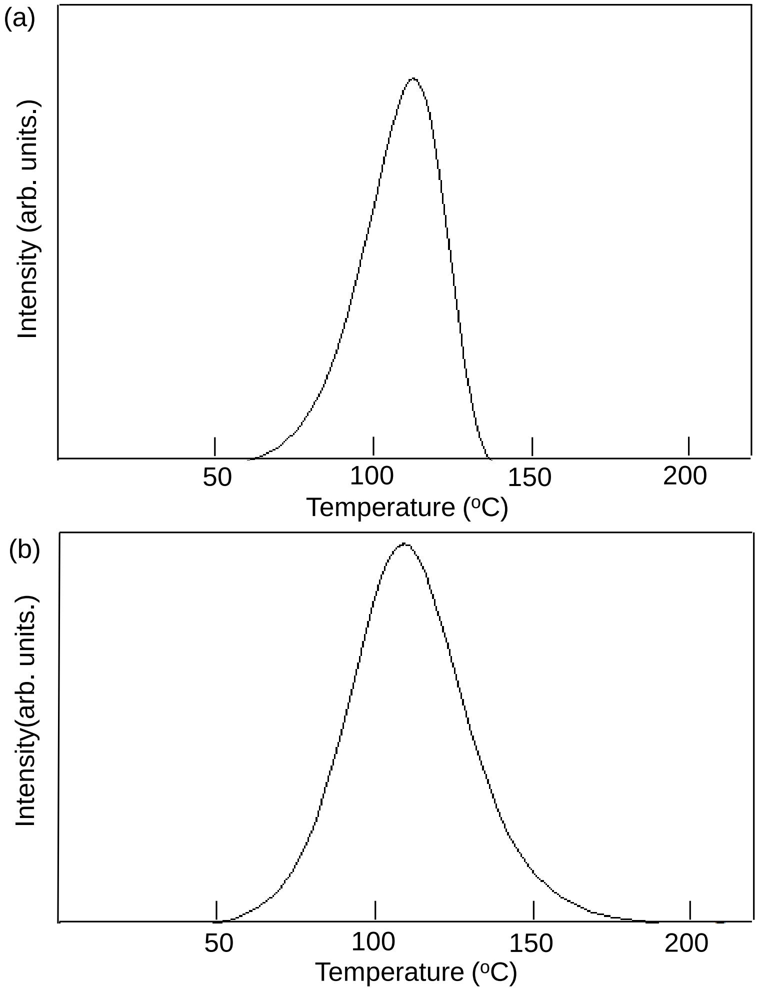

Figure 2.9 (a) First-order and (b) second-order thermoluminescence curves calculated using equations (2.6) and (2.7). The parameters are E = 1.5 eV, $s = 10^{12}$ s^{-1}, n_0 = N= 10^3 m^{-3}.

CHAPTER 3

NEAR-INFRARED LONG-PERSISTENT LUMINESCENCE IN Cr^{3+}-DOPED Ga_2O_3 NANOWIRES

3.1 Introduction

Gallium oxide (Ga_2O_3) is a wide-bandgap (~4.9 eV) semiconductor which provides the opportunity to tune the emission wavelengths between ultraviolet and infrared when foreign impurities are introduced. Ga_2O_3 nanowires have been reported to emit characteristic UV[72] and blue light[73]. It has been suggested that the UV emission is due to the recombination of a self-trapped exciton, while the blue emission results from the recombination of a trapped electron in a donor with a trapped hole in an acceptor[74]. Oxygen vacancies act as the shallow donors and the acceptors should be pair of gallium and oxygen vacancies[74]. Ga_2O_3 nanowires can also emit red light when doped with chromium[75] or nitrogen[76]. However, no persistent NIR luminescence was observed in nanowires before. In this chapter, we report persistent NIR luminescence from Cr^{3+}-doped β-Ga_2O_3 nanowires synthesized by a hydrothermal process followed by calcination. The β-Ga_2O_3:Cr^{3+} nanowires exhibit persistent luminescence in the 650–850 nm wavelength range with an afterglow time of more than 4 h at room temperature.

3.2 Sample preparation and characterization

Cr^{3+}-doped Ga_2O_3 nanowires were synthesized by the hydrothermal method. In a typical synthesis, 7 ml, 4 M NaOH aqueous solution was added dropwise into 11 ml, 0.2 M $GaCl_3$ aqueous solution under vigorous stirring to form white colloidal precipitates. 0.02 ml, 0.05 M $Cr(NO_3)_3$ aqueous solution and 0.14 g $Ca(NO_3)_2 \cdot 4H_2O$ powder were then added to the colloidal suspension under stirring. The resulting solution was transferred into a Teflon-lined stainless steel autoclave and heated at 180 ℃ in an oven for 24 h. After the reaction, the white product was separated by centrifugation, washed with deionized water and pure alcohol for several times, and dried at 80 ℃ in an oven for overnight. After subsequent calcination at 900 ℃ in air for 2 h, pure β-Ga_2O_3:Cr^{3+} was obtained. The influence of Ca^{2+} ions concentration on the morphology of the final products was also investigated by adding various amounts of $Ca(NO_3)_2 \cdot 4H_2O$ (0g, 0.01 g, 0.035 g, and 0.14 g), while keeping the other synthetic conditions unchanged.

The crystal structure of the as-synthesized materials were analyzed by an X-ray diffractometer (XRD, PANalytical) with CuKα radiation. The morphology and crystal structures were measured by a field emission gun scanning electron microscope (SEM, FEI Inspect F) and a transmission electron microscope (TEM, Hitachi HF-3300 STEM). The compositions were analyzed by an energy-dispersive x-ray spectroscopy (EDS, EDAX GENESIS XM 2) attached to the Inspect FSEM.

The optical properties of the as-synthesized phosphors were measured using a spectrofluorometer (Horiba Fluorolog-3) equipped with a 450 W Xenon lamp, a standard R928P photomultiplier tube (240-850 nm) and an extended, liquid nitrogen-cooled DSS-IGA020L InGaAs detector (800-1600 nm). The data acquired include photoluminescence emission and excitation spectra, afterglow spectra, afterglow decay curves, and thermoluminescence spectra. To measure the photoluminescence at 77 K, a Dewar flask filled with liquid nitrogen was used to freeze and maintain the temperature of the sample. The Dewar flask is placed on a pedestal which can fit into the T-box sample compartment module of the Horiba spectrofluorometer. NIR afterglow photos of the samples were taken in darkness using a digital camera connected with an ITT PVS-14 night vision monocular (with a GaAs photocathode) at different delay times after removal of the irradiation sources. The irradiation sources include 4-W UV lamps (254 nm or 365 nm) and a 450-W Xenon lamp. Thermoluminescence curves were acquired on a home-made thermoluminescence measurement set-up. The thermoluminescence measurement system is made up of two parts (see **Figure 2.8**): one is the Fluorolog-3 spectrofluorometer and the other is a heating system which can perform the linear heating rate. The schematic diagram of heating system is shown in **Figure 3.1**. For the heating system, since the thermoluminescence peak corresponding to the suitable trap depth should locate in the range around or above room temperature, the system was designed to operate from room temperature to 300 ℃. In order to minimize the temperature gradient between the sample and the heater, copper was used as the sample holder because of its excellent thermal conductivity. The sample holder is a cuboid which 1.5 cm long, 2 cm wide and 3 cm high. A shallow hole with diameter of 2 cm was drilled on one side of the Cu cuboid for loading sample, and two holes were drilled on the top for mounting a 50 W cartridge heater and a type-K thermocouple. To accurately control the sample temperature, the positions of the thermocouple, sample and heater are designed to be very close. The whole setup can fit into the sample compartment of the Fluorolog-3 spectrofluorometer. In order to correctly analyze the thermoluminescence curve, a linear heating rate is required. To do so, the temperature is controlled by a programmable Omega CN 9600 temperature controller. Before measurement, the traps of the sample need to be emptied. These traps were previously filled due to the exposure of the sample to the room light. Empting these traps was accomplished by heating the sample at around 350 ℃ in a muffle furnace. After cooled to room temperature naturally, the sample was irradiated under the desired wavelength using either UV lamps or a Xenon lamp for an appropriate time. After stoppage of the irradiation, the afterglow decay curves and thermoluminescence signals were recorded by the Fluorolog-3 spectrofluorometer in the kinetic mode.

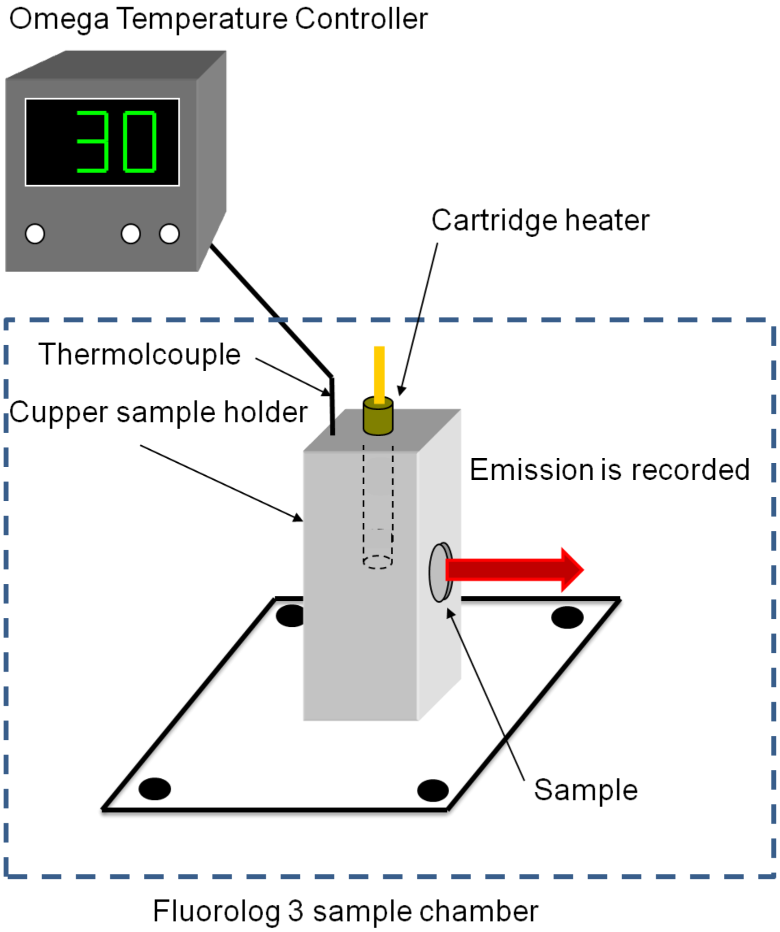

Figure 3.1 Schematic diagram of the thermoluminescence measurement set-up.

3.3 Structure and morphology of Cr^{3+}-doped Ga_2O_3 nanowires

Figure 3.2a shows the XRD pattern of the white product prepared with the addition of 0.14 g $Ca(NO_3)_2 \cdot 4H_2O$ powder into the 7 ml NaOH and 11 ml $GaCl_3$ solution, which is in good agreement with the standard pattern of α-GaOOH (JCPDS 06-0180). This means that the hydrothermal product is α-GaOOH. After subsequent calcination at 900 °C in air for 2 h, pure monoclinic β-Ga_2O_3 (JCPDS 41-1013) was obtained (**Figure 3.2b**). No peaks related to Ca-containing phases were detected within the detection limit of the XRD. β-Ga_2O_3 is the most stable form of gallium oxide [77].

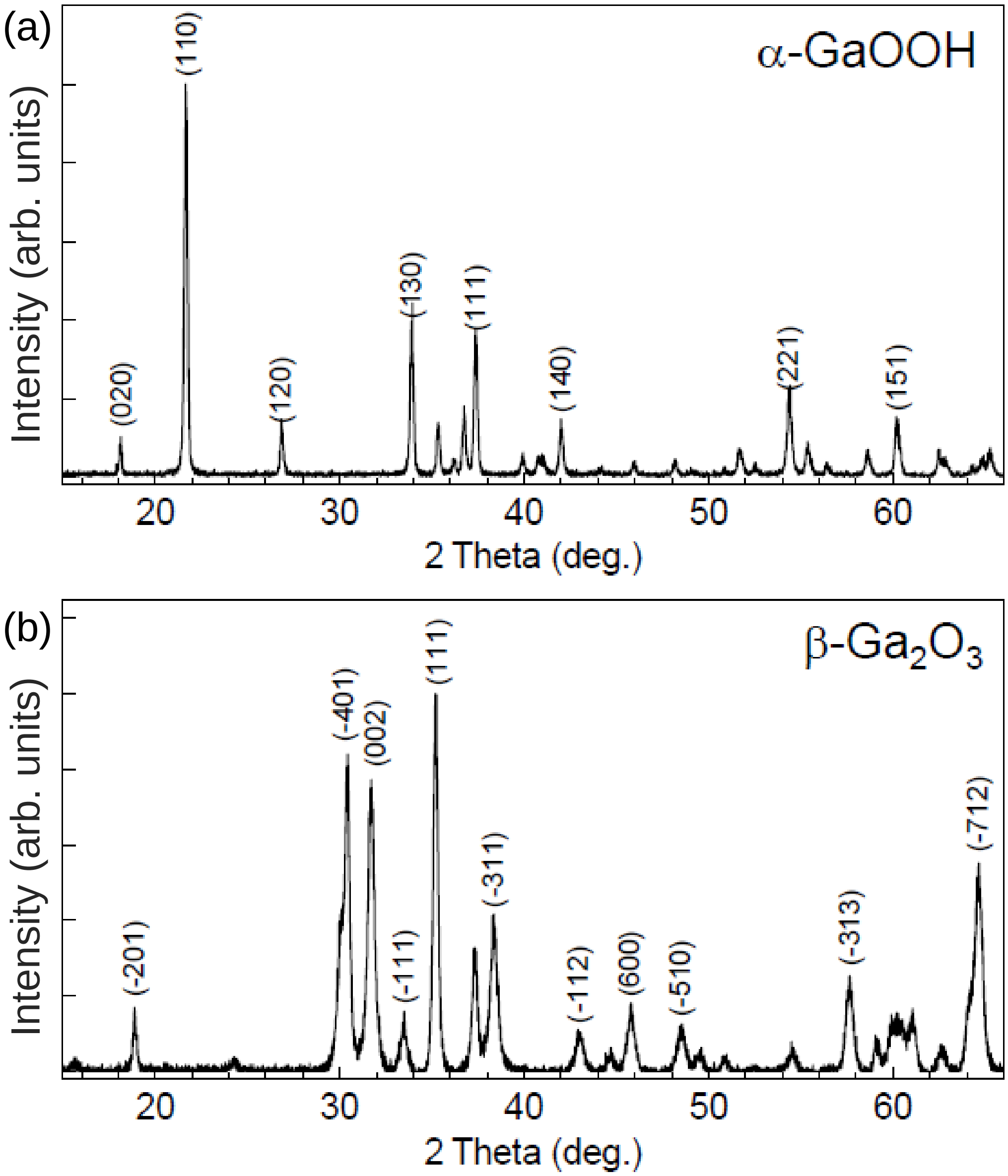

Figure 3.2 XRD patterns of (a) α-GaOOH nanowires and (b) β-Ga_2O_3 nanowires.

Scanning electron microscopy (SEM; **Figure 3.3a**) and transmission electron microscopy (TEM; **Figure 3.3b**) observations showed that the α-GaOOH crystals prepared with the addition of 0.14 g $Ca(NO_3)_2 \cdot 4H_2O$ powder into the 7 ml NaOH-11 ml $GaCl_3$ solution are present in the form of nanowires with diameters of 50–80 nm and lengths of up to 8 μm. One unique growth phenomenon for α-GaOOH nanowires is that tens of nanowires tend to assemble into spindle-like morphology (**Figure 3.3a**), which was also observed by other groups[72,78]. After the calcination, the orthorhombic α-GaOOH nanowires were converted to monoclinic β-Ga_2O_3 nanowires (**Figure 3.2b**), whilst the morphology and size of the nanowires and nanowire assemblies were reserved, as the images shown in **Figure 3.3c,d**.

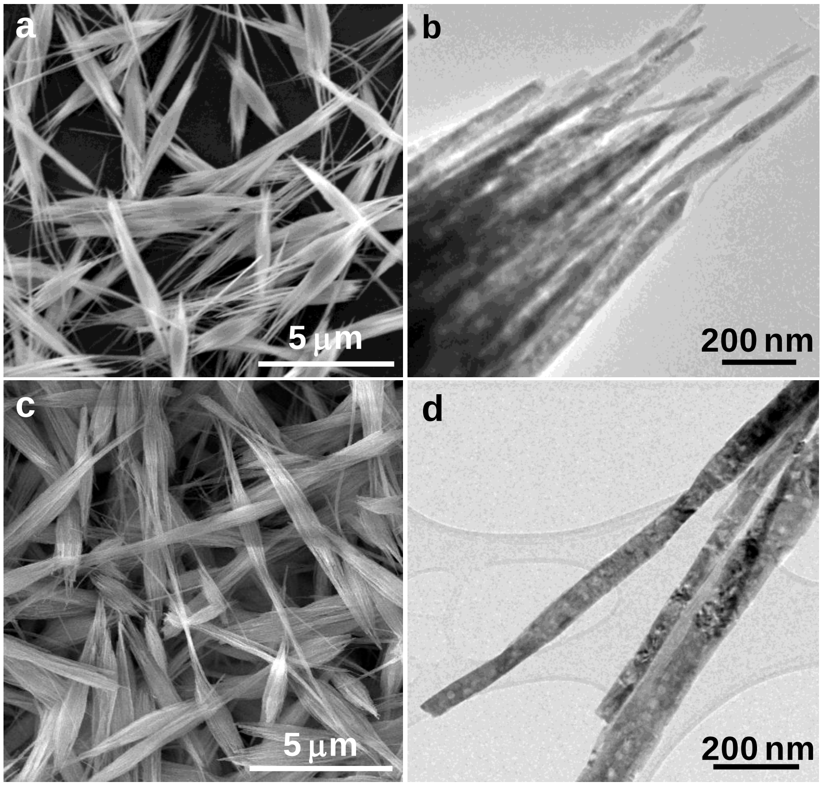

Figure 3.3 (a) SEM image of spindle-like α-GaOOH:Cr^{3+} nanowire assemblies. (b) TEM image of α-GaOOH:Cr^{3+} nanowires. (c) SEM image of spindle-like β-Ga_2O_3:Cr^{3+} nanowire assemblies. (d) TEM image of β-Ga_2O_3:Cr^{3+} nanowires.

In our synthesis, we found that the concentration of Ca^{2+} ions have significant influence on the morphologies of the final products. For the samples synthesized without Ca^{2+} ions, spindle-like α-GaOOH consisting of irregular nanorods with varied length and width (**Figure 3.4a**) is obtained. After adding 0.01 g of $Ca(NO_3)_2 \cdot 4H_2O$, the product is still spindle-like nanorod assemblies, however, the nanorods become thinner and longer (**Figure 3.4b**). When the amount of $Ca(NO_3)_2 \cdot 4H_2O$ increases to 0.035 g, more oriented parallel nanorods with much smaller diameter are formed (**Figure 3.4c**). Further increase of the amount of $Ca(NO_3)_2 \cdot 4H_2O$ to 0.14 g results in the formation of fairly uniform spindlie-like α-GaOOH:Cr^{3+} nanowire assemblies, as shown in **Figure 3.4d**. The nanowires in **Figure 3.4d** are acyually the same as those shown in the **Figure 3.3a**. These images show that with the increase of Ca^{2+} concentration, the morphology of the α-GaOOH products changes from short nanorod bundles to long nanowire

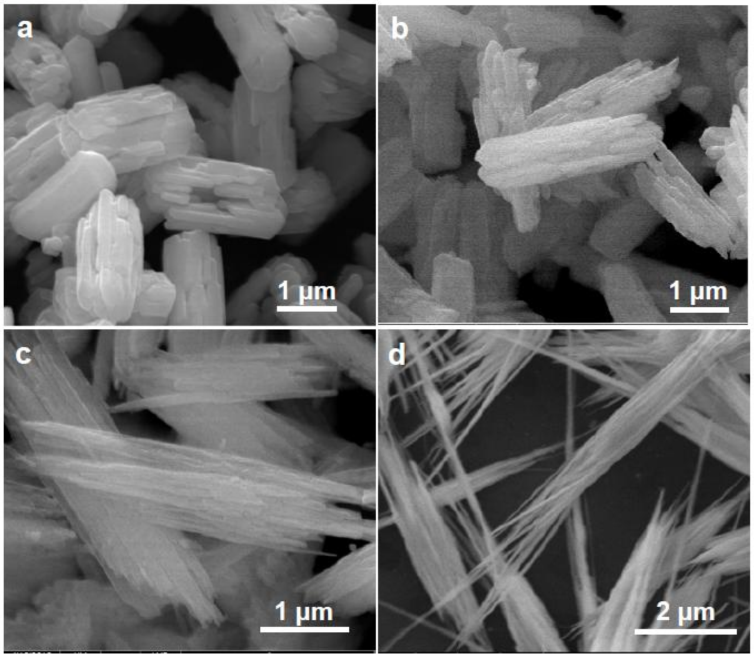

Figure 3.4 SEM images showing the effects of Ca^{2+} concentration on the morphology of α-GaOOH nanostructures. The amount of $Ca(NO_3)_2 \cdot 4H_2O$ powder added to the 7 ml NaOH and 11 ml $GaCl_3$ solution is (a) 0, (b) 0.01 g, (c) 0.035 g, and (d) 0.14 g.

bundles. The EDS spectrum (**Figure 3.5**) shows that only Ga and O were detected in the sample, which further supports the results of XRD measurements. The concentration of Cr^{3+} is too low (<0.1 atom%) to detected by EDS.

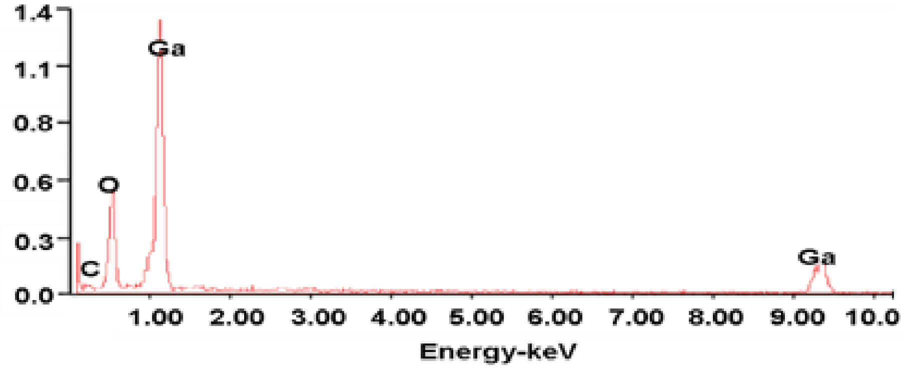

Figure 3.5 Energy-dispersive X-ray spectroscopy spectrum of β-$Ga_2O_3:Cr^{3+}$ nanowires.

In hydrothermal synthesis of spindle-like α-GaOOH:Cr^{3+} assemblies, alkali ions and surfactants were used to control the morphology of the α-GaOOH:Cr^{3+} nanostructures. Currently, the mechanism of the morphological evolution with the presence of these additives is not clear. However, it is generally believed that these additives adsorbed on the surface of the nanocrystals and thus influence their growth behaviors.[79]

3.4 Photoluminescence properties

Figure 3.6 shows the normalized excitation and emission spectra of β-$Ga_2O_3:Cr^{3+}$ nanowires at room temperature. Under excitation at 300 nm, there are two clear R lines (R_1 lineat 696 nm and R_2 line at 688 nm) superimposing on a broadband centered at 711 nm in the emission spectrum. The R lines and broadband emissions can be, respectively, assigned to $^2E \rightarrow {}^4A_2$ and $^4T_2 \rightarrow {}^4A_2$ transitions[58]. The coexistence of the R lines and broadband emissions suggests that Cr^{3+} ions locate in intermediate field[58,80,81]. This result clearly demonstrates that the

Cr^{3+} ions are doped into β-Ga_2O_3 and substitute Ga^{3+} ions in the distorted octahedral sites of β-Ga_2O_3. The excitation spectrum of β-Ga_2O_3:Cr^{3+} monitored at 720 nm consists two characteristic Cr^{3+} broad bands with peaks at 437 nm ($^4A_2 \rightarrow {}^4T_1$(F) transition) and at 609 nm ($^4A_2 \rightarrow {}^4T_2$ transition).

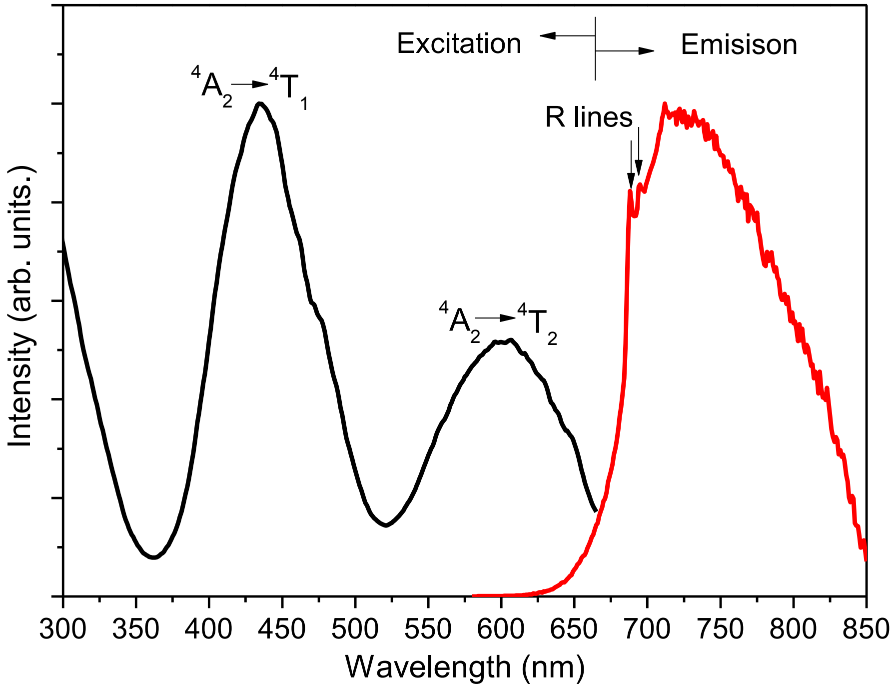

Figure 3.6 Normalized excitation and emission spectra of β-Ga_2O_3:Cr^{3+} nanowires. The emission spectrum is acquired under 300 nm light excitation and the excitation spectrum is obtained by monitoring at 720 nm emission.

We also measured the emission spectra of β-Ga_2O_3:Cr^{3+} prepared with the presence of different amount of Ca^{2+} ions (0 g, 0.01 g, 0.035 g and 0.14 g) during the hydrothermal process, as that shown in **Figure 3.7**. It is clear that even though the Ca^{2+} ions can significantly alter the morphology of the initial Ga(OOH) products, it doesn't affect the optical properties of the final β-Ga_2O_3:Cr^{3+} nanostructures.

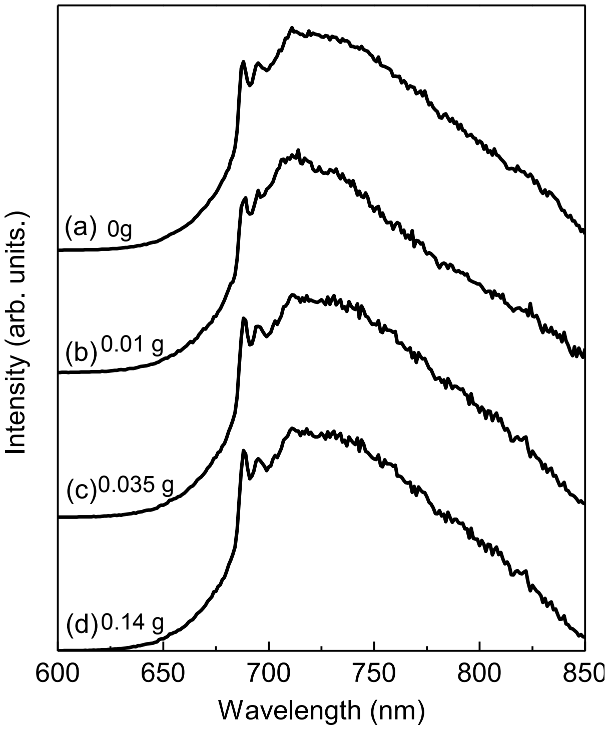

Figure 3.7 Emission spectra of β-Ga_2O_3:Cr^{3+} prepared by adding (a) 0, (b) 0.01 g, (c) 0.035 g, and (d) 0.14 g of $Ca(NO_3)_2 \cdot 4H_2O$ into a 7 ml NaOH and 11 ml $GaCl_3$ solution. The emission spectrum is acquired under 300 nm light excitation at room temperature.

Figure 3.8 shows the normalized emission spectra of β-Ga_2O_3:Cr^{3+} nanowires under 300 nm excitation at 77 K and 300 K. At 77 K, two R lines dominate accompanying with their phonon sideband. This reveals that the $^4T_2$ emission is greatly depressed at 77 K. At room temperature, however, the $^4T_2 \rightarrow {}^4A_2$ transition dominates the emission. The comparison of these two emission spectra reveals that there is a significant variation in intensity ratio of broadband emission to the R line emission with temperature. The energy gap between the ^2E and $^4T_2$ levels in β-Ga_2O_3:Cr^{3+} is sufficiently small that allows a thermal population of the $^4T_2$ states at room temperature, resulting in the coexistence of the R line and the pronounced $^4T_2 \rightarrow {}^4A_2$ broadband emission. At low temperature, however, the lower excited level (^2E) would be the exclusive emitting level.

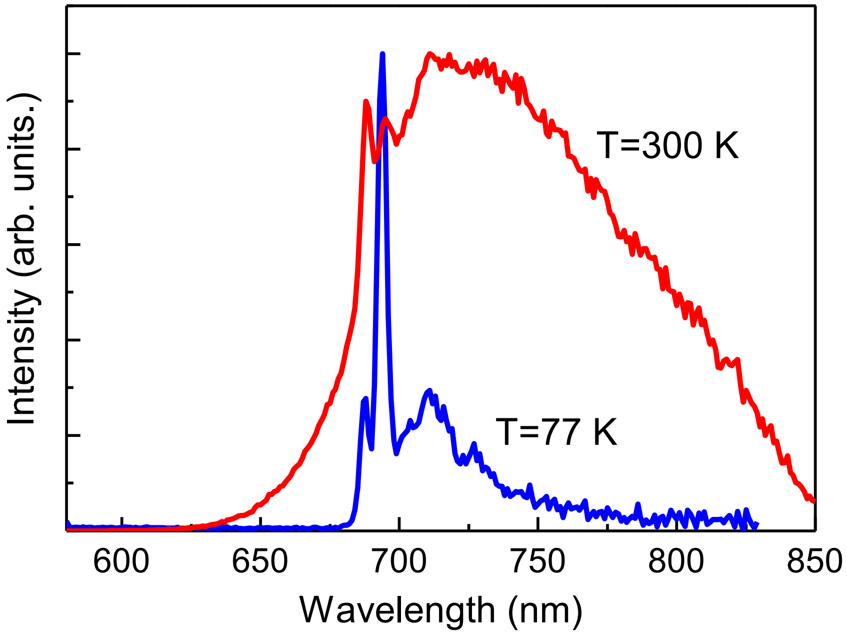

Figure 3.8 Normalized photoluminescence emission spectra of β-Ga_2O_3:Cr^{3+} nanowires excited at 300 nm at T= 300 K and 77 K.

3.5 Long-persistent luminescence investigation

Besides NIR photoluminescence, the β-Ga_2O_3:Cr^{3+} nanowires also exhibit long-persistent NIR luminescence after the removal of the excitation source. **Figure 3.9** gives the afterglow decay curve of the β-Ga_2O_3:Cr^{3+} nanowires monitored at 720 nm after irradiated by 300 nm light (from a 450 W Xenon lamp) for 10 min. The persistent NIR emission lasts for more than 4 h. We also measured the emission spectra during the afterglow process. The inserted curve in **Figure 3.9** is the afterglow spectrum recorded at 1 h after the irradiation. The good agreement of the the spectral profiles between the photoluminescence spectrum (**Figure 3.6**) and the afterglow spectrum (inset of **Figure 3.9**) indicates that the afterglow exists in the whole spectral region of the photoluminescence emission band. The long NIR afterglow was also monitored and imaged by a PVS-14 night vision monocular. The photos inserted in **Figure 3.9** are the afterglow images of ~0.1 g β-Ga_2O_3:Cr^{3+} nanowires taken in a dark room at 15 s and 1 h after the stoppage of the irradiation. The NIR afterglow is detectable to the monocular for more than 4 h, which is consistent with the decay measurement.

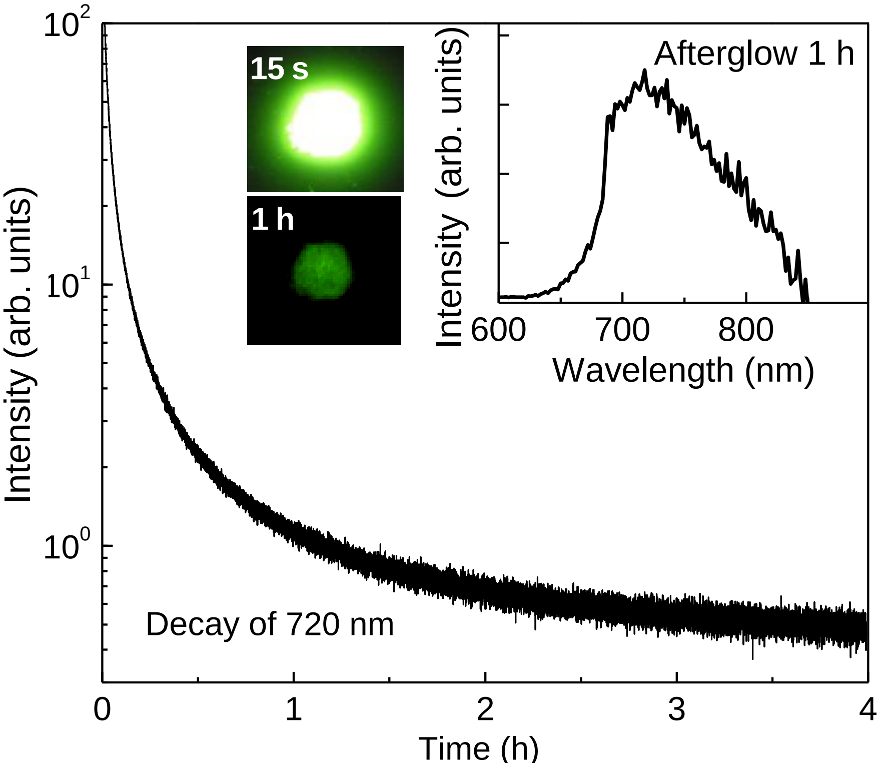

Figure 3.9 Afterglow decay curve of β-Ga_2O_3:Cr^{3+} nanowires monitored at 720 nm. The inserted curve is the afterglow (at 1 h) spectrum. The inserted images are the afterglow photos taken at 15 s and 1 h by a digital camera via a night vision monocular in a dark room. Before measurement and imaging, the samples were excited by a UV lamp (at 254 nm) for 10 min.

Although the photoluminescence of the β-Ga_2O_3:Cr^{3+} phosphor can be effectively excited by wide range of energies (see **Figure 3.6**), the situation for the NIR afterglow can be different because of the different activation mechanisms between the photoluminescence and afterglow. To evaluate the effect of different excitation energies on the NIR afterglow, we study the afterglow characteristics of the β-Ga_2O_3:Cr^{3+} phosphor under the irradiation in a wide range of excitation energies (from UV to red) using the Fluorolog-3 spectrofluorometer.

In the evaluation of the excitation energy-afterglow relationship, the following two conditions were followed. (1) To avoid the influence of the fast early decay on the analysis of afterglow, the afterglow intensity values at the I_{1s} points under different excitation energies were compared. The point of I_{1s} represents the afterglow intensity recorded at time of 1 s after the stoppage of the irradiation. (2) To all excitation energies, the afterglow was monitored at the same wavelength (696 nm in present study). This is because for the same persistent phosphor, a certain afterglow wavelength is supposed to correspond to particular emitting centers and traps, which allows for fairly evaluating the effectiveness of different excitation energies. **Figure 3.10** shows the I_{1s} values monitored at 696 nm as a function of excitation wavelengths. The photoluminescence excitation spectrum monitored at 696 nm is also given in **Figure 3.10** for comparison. **Figure 3.10** clearly shows that the NIR afterglow can be effectively achieved under UV illumination (~300-370 nm) but is barely achieved by green light (~520 nm) irradiation.

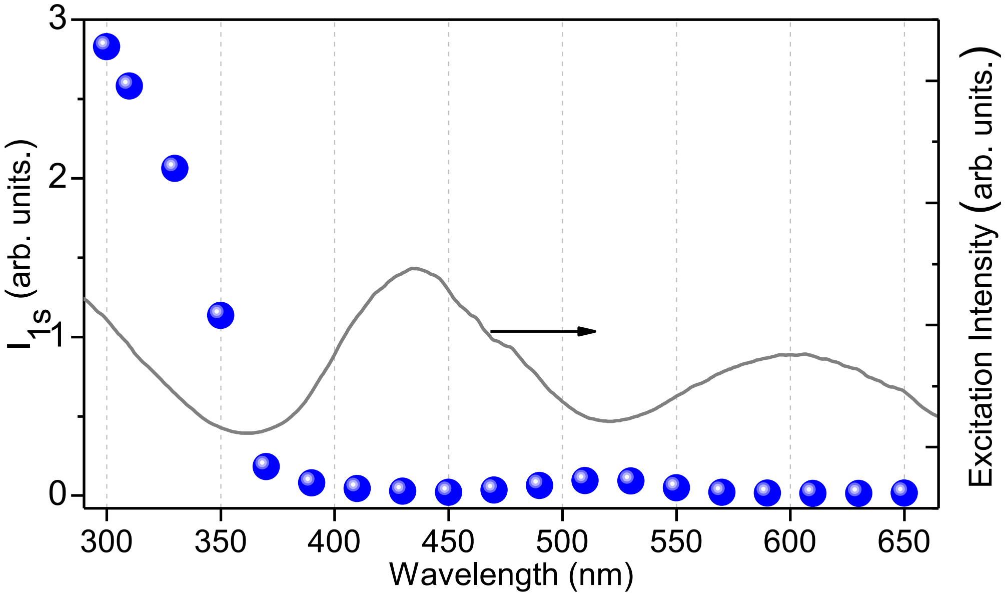

Figure 3.10 Afterglow intensity of β-Ga_2O_3:Cr^{3+} nanowires monitored at 696 nm emission as a function of the irradiation energy (represented by balls). The solid line curve is the photoluminescence excitation spectrum monitored at 720 nm.

Furthermore, the photoluminescence excitation energy peaked at ~440 nm (blue) and ~660 nm (red) is completely inactive to the NIR afterglow. Note that although the afterglow behaviors at different emission wavelengths may be different in the β-Ga_2O_3:Cr^{3+}, the irradiation energy dependences of afterglow intensities monitored at different emission wavelengths, i.e., from 650 nm to 850 nm, show the similar evolutions as that shown in **Figure 3.10**.

3.6 Thermoluminescence investigation

Figure 3.11 shows the thermoluminescence curves monitored at 720 nm with irradiation times of 5 s, 20 s and 10 min. The irradiation wavelength is 300 nm from a Xe lamp. With the increase of the irradiation time, the maximum intensities of the three curves do not shift to higher temperature suggesting that they are first-order kinetics[64].

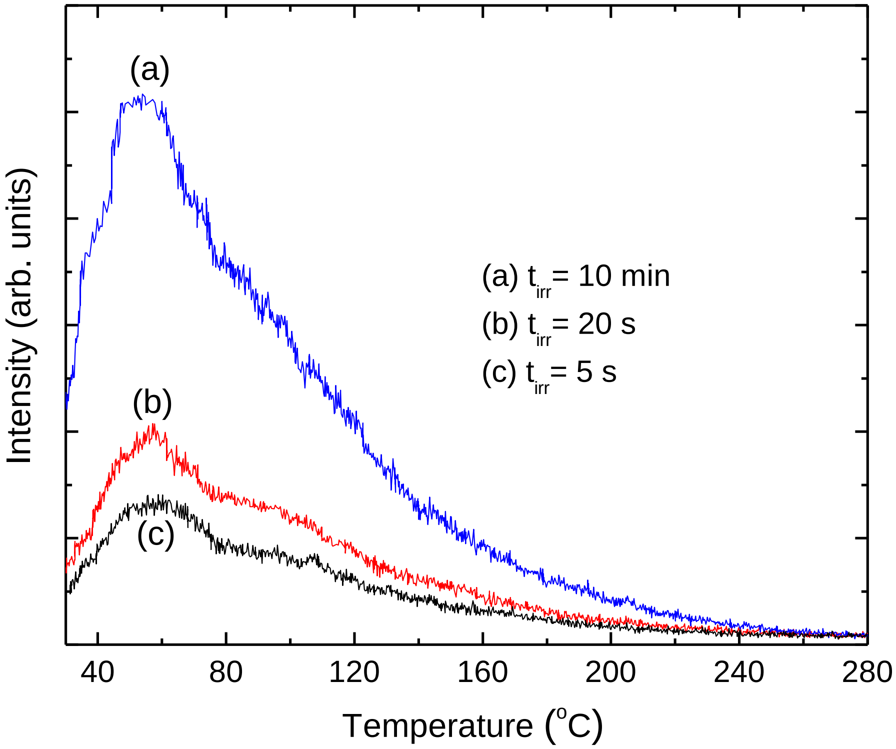

Figure 3.11 Thermoluminescence curves of β-Ga_2O_3:Cr^{3+} nanowires monitored at 720 nm after exposed to 300 nm irradiation for (a) 5 s, (b) 20 s, and (c) 10 min.

To learn the distribution of the traps in β-Ga_2O_3:Cr^{3+} nanowires, we conducted thermoluminescence measurements with different delayed times after the stoppage of the irradiation. **Figure 3.12** shows the thermoluminescence curves monitored at 720 nm with delay times of 10 s and 30 min after ceasing the irradiation (300 nm for 10 min). The curve recorded with delay time of 10 s shows an asymmetric broad band covering from 25 °C to ~250 °C. When the delay time increases to 30 min, the low-temperature band (25 °C to ~100 °C) disappears and the high-temperature band (~50 °C to ~250 °C) still exists, indicating that the shallow traps are emptied. The difference between the 10 s and 30 min curves, which is represented by the dashed line curve in **Figure 3.12**, reveals the existence of at least two traps with different trapping depths in β-Ga_2O_3:Cr^{3+}: low-temperature shallow trap and high-temperature deep trap[30], with the latter one being mainly responsible for the long afterglow of the persistent NIR luminescence.

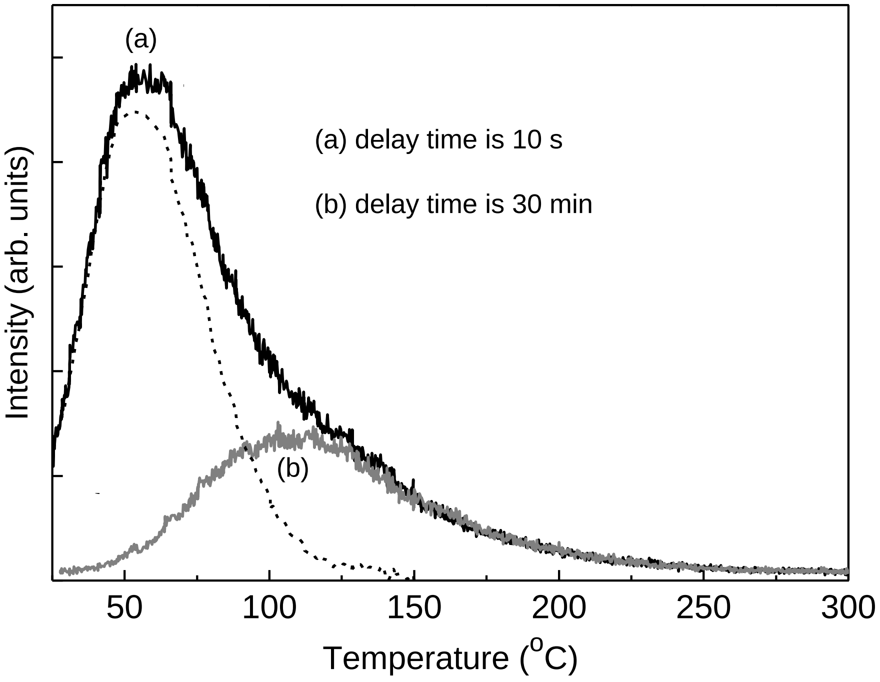

Figure 3.12 Thermoluminescence curves of β-Ga_2O_3:Cr^{3+} nanowires monitored at 720 nm with delay times of 10 s and 30 min after ceasing the irradiation of a xenon lamp (at 300 nm for 10 min). Dashed line curve is the difference between the 10 s and 30 min curves.

3.7 Long-persistent luminescence mechanism

Based on the above results and analyses, the persistent NIR luminescence process is proposed and illustrated in **Figure 3.13**. Initially, Cr^{3+} ions are excited under external irradiation. Part of the excited electrons is captured by the traps, e.g., oxygen vacancies, which locate in the vicinity of the Cr^{3+} ions in the β-Ga_2O_3 host. When the trapped electrons are thermally released and recombine with the holes located at the ionized Cr^{3+} ions, the excited level of the Cr^{3+} ions, e.g., $^4T_1(te^2)$, is populated again. Subsequently, long persistent NIR emission occurs from the ^2E and $^4T_2$ emitting levels, which correspond, respectively, to the R lines and broadband emissions.

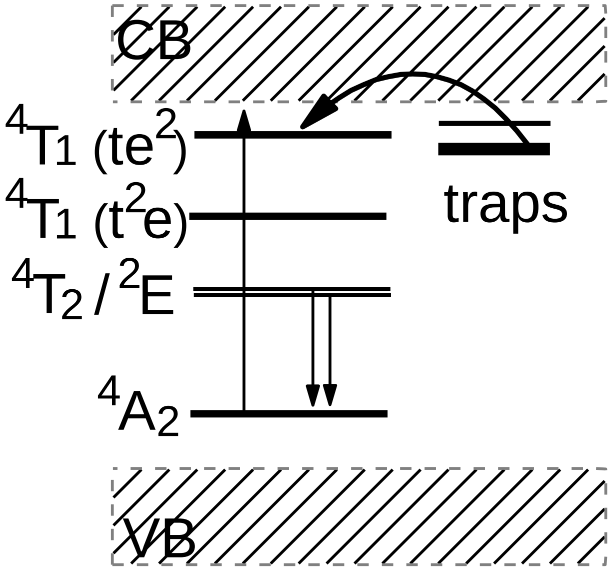

Figure 3.13 Schematic diagram of the persistent NIR luminescence mechanism of β-Ga_2O_3:Cr^{3+} nanowires. The straight line arrows and curved line arrow represent the optical transitions and electron transfer process, respectively.

3.8 Summary

In summary, we reported the first NIR persistent luminescence nanowires, β-Ga_2O_3:Cr^{3+} nanowires, with persistence time of more than 4 h. The NIR long-persistent luminescence can be effectively achieved under UV illumination (~250-370 nm), but is barely achieved by blue light (480 nm), even though the blue light excitation are effective to the NIR photoluminescence. The NIR afterglow mechanisms were studied by measuring thermoluminescence cures and the irradiation energy dependence of the afterglow intensity. Such long afterglow time, along with the invisible (to naked eyes) nature of the NIR emission and the small size of the nanowires, make the β-Ga_2O_3:Cr^{3+} nanowires very suitable for many important applications, e.g., as taggants in defense and security, and as optical probes for *in vivo* deep tissue bio-imaging.

CHAPTER 4

SOLAR RADIATION-ACTIVATED NEAR-INFRARED LONG-PERSISTENT LUMINESCENCE IN Cr^{3+}-DOPED ZINC GALLOGERMANATES

4.1 Introduction

In this chapter, we report super-long lasting NIR persistent luminescence with persistence time of up to 400 h achieved from Cr^{3+}-doped zinc gallogermanate series of phosphors. Such long persistent time is more than two orders of magnitude longer than previously reported NIR persistent phosphors[51,52]. Remarkably, the Cr^{3+}-doped zinc gallogermanates can be quickly, effectively and repeatedly charged by sunlight at any weather conditions, at any moment between sunrise and sunset, at any outdoor locations, and in various aqueous solutions.

4.2 Sample preparation and characterization

The general chemical formula of the Cr^{3+}-doped zinc gallogermanates can be written as $Zn_xGa_yGe_zO_{(x+(3y/2)+2z)}$:$t$$Cr^{3+}$, mR, where R is a co-dopant selected from a group consisting of alkaline earth ions, lanthanide ions, and Li^+ ions; x, y, and z are integers from 1 to 5; t is 0.01 mol% to 2 mol% based on the total moles of Ga; and m is 0 to 2 mol% based on the total moles of Ga. In addition, Ga can be partially replaced with an IIIA metal ion (e.g., In^{3+}) or Ge^{4+} can be partially or fully substituted with an IVA metal ion (e.g., Sn^{4+}) in the matrix. Any combinations of these variables can always produce materials with remarkable NIR persistent luminescence. In this chapter, we focus our discussion on chemical formula of $Zn_3Ga_2Ge_4O_{14}$:0.1%Cr^{3+} to show the superb capabilities of the Cr^{3+}-doped zinc gallogermanates in excitation energy absorption, storage, NIR light conversion, and NIR light persistent luminescence. The influence of the host composition, Cr^{3+} ion concentrations and co-dopant on the optical properties of the phosphors will also be discussed where appropriate.

The Cr^{3+}-doped zinc gallogermanates was synthesized by the solid-state reaction method. Stoichiometric amount of ZnO, Ga_2O_3, GeO_2, and Cr_2O_3 powders were milled or ground to form a homogeneous fine powder for pre-firing. The mixed powder was then prefired at 900 °C in air for 2 h. The pre-fired material was again ground to fine powder suitable for sintering. Part of prefired powder was pressed into ceramic disks with diameters varying from 15 mm to 75 mm. The disks were then sintered at 1250 °C in air for 2 h, while the powder samples were sintered at 1100 °C in air for 2 h.

The optical properties of the as-synthesized phosphors were measured using a spectrofluorometer (Horiba Fluorolog-3) equipped with a 450 W Xenon lamp, a standard R928P photomultiplier tube (240-850 nm) and an extended, liquid nitrogen-cooled DSS-IGA020L InGaAs detector (800-1600 nm). Thermoluminescence curves were taken on a home-made thermoluminescence measurement set-up. The configuration and functions of the thermoluminescence measurement set-up were described in detail in Chapter 2 and Chapter 3. In fluorescence lifetime measurements, a YAG pumped dye laser was used as an excitation source, and the signals were synchronously detected and averaged with a TDS 460A Digitizing oscilloscope from Tektronix. The dye system was pumped at 532 nm with the second harmonic of a YAG:Nd laser.

NIR afterglow photos of the samples were taken in darkness using a digital camera via an ITT PVS-14 night vision monocular (with a GaAs photocathode) at different delay times after removal of the irradiation sources. The irradiation sources include a 450-W Xenon lamp equipped in the Fluorolog-3 spectrofluorometer, two 4-W ultraviolet (UV) lamps at 254 nm and 365 nm, and the natural sunlight.

4.3 Photoluminescence properties

Figure 4.1 shows the normalized excitation and emission spectra of the $Zn_3Ga_2Ge_4O_{14}$:0.1%Cr^{3+} phosphors at room temperature. The excitation spectrum covers almost the whole UV-visible spectral region and consists of two main excitation bands originated from the inner transitions of Cr^{3+} ions, including the 404 nm band originated from the $^4A_2 \rightarrow {}^4T_1(t^2e)$ transition, and the 570 nm band originated from the $^4A_2 \rightarrow {}^4T_2(te^2)$ transition. Under excitation at 400 nm, the material exhibits characteristic emission from Cr^{3+} ions, featuring a broadening R line at 696 nm (attributed to $^2E \rightarrow {}^4A_2$ transition of Cr^{3+}) superimposing on an emission band from 700-850 nm. The broadening R line emission suggests that the Cr^{3+} ions experience disorder-

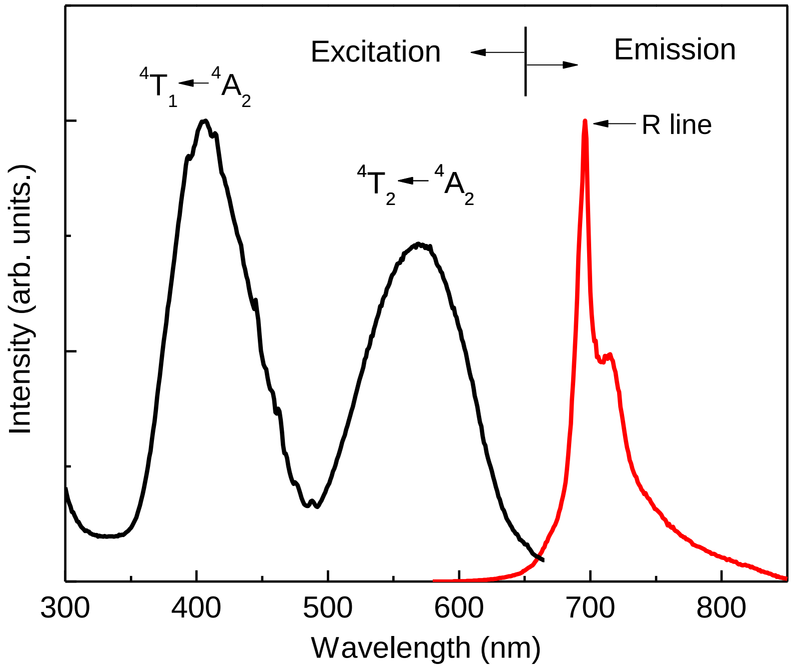

Figure 4.1 Normalized excitation and emission spectra of $Zn_3Ga_2Ge_4O_{14}$:0.1 % Cr^{3+} at room temperature. The emission spectrum is acquired under 400 nm light excitation and the excitation spectrum is obtained by monitoring at 696 nm emission.

induced distribution of crystal field strength in the host lattice[82-85]. To obtain more information about the broadband emission (700-850 nm) of $Zn_3Ga_2Ge_4O_{14}$:0.1%Cr^{3+}, room-temperature fluorescence lifetime of Cr^{3+} emission monitored at different wavelengths were recorded and studied. The fluorescence lifetime curves under a 585 nm laser excitation were plotted in **Figure 4.2**. The monitored wavelengths were selected within both the R line and broadband portions of emission spectrum (696 nm, 730 nm, 750 nm and 780 nm). One can see that except for the fluorescence lifetime monitored at 696 nm, the other curves are non-exponential. The non-exponential behavior strongly suggests that the Cr^{3+} ions sit in multi-sites of different crystal fields[86,87]. The lifetime of the fast decay part is estimated to be 550 μs by fitting the curve and

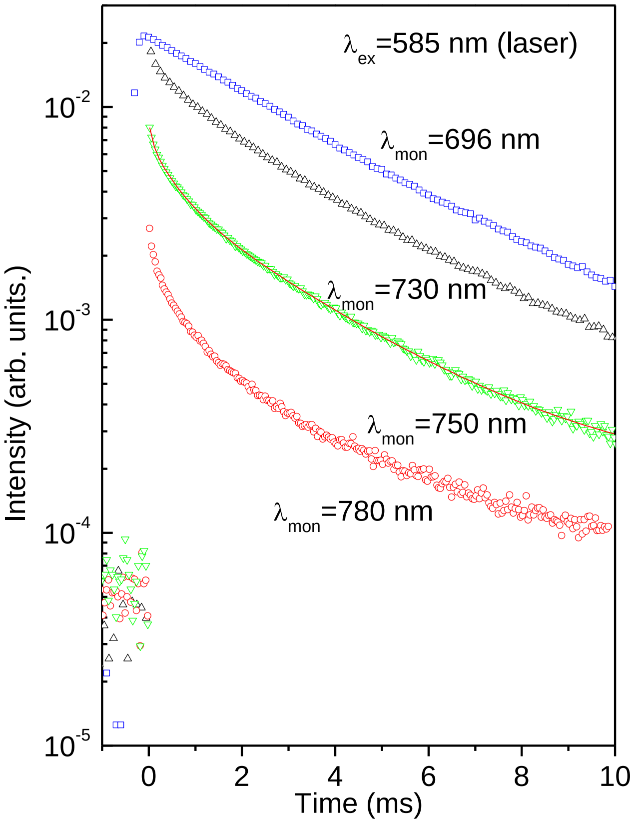

Figure 4.2 Fluorescence lifetimes monitored at 696 nm, 730 nm, 750 nm, and 780 nm emissions in $Zn_3Ga_2Ge_4O_{14}$:0.1%Cr^{3+} at room temperature. A 585 nm laser is used as the excitation source.

is in agreement with the lifetime of $^4T_2 \rightarrow ^4A_2$ transition, which is of the order of microseconds[88]. At latter times, the decay curve becomes a single exponential with lifetime around 3.5 ms, which is a long lifetime characteristic of R line emission[88]. The fast decay portion dominated more with the increase of the emission wavelengths. This phenomenon suggests that the broadband emission contains $^4T_2 \rightarrow ^4A_2$ transition. Furthermore, we can't exclude the contribution from R line phonon sidebands to the broad emission band.

4.4 Long-persistent luminescence invesitgation

The Cr^{3+}-doped zinc gallogermanates exhibit super-long lasting NIR persistent luminescence after the removal of the excitation source. **Figure 4.3** shows the persistent luminescence decay curve of $Zn_3Ga_2Ge_4O_{14}$:0.1%Cr^{3+} phosphors monitored at 696 nm after irradiated by a 365 nm UV lamp for 10 min. The data was recorded as persistent luminescence intensity versus time and the recording last for 24 h. It is clear that after 24 h persistent emission, the luminescence intensity of the sample is still very strong.

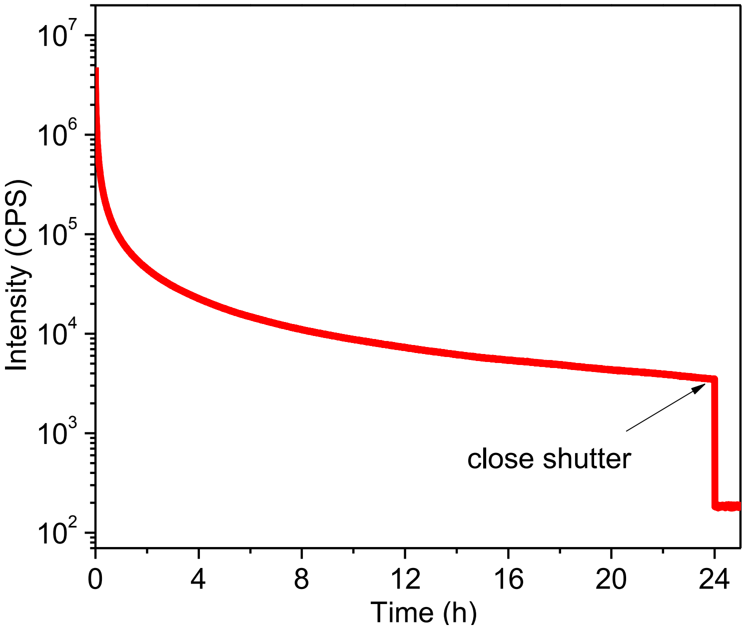

Figure 4.3 Afterglow decay curve of $Zn_3Ga_2Ge_4O_{14}$:0.1%Cr^{3+} monitored at 696 nm after irradiation by a 365 nm UV lamp for 10 min.

We also measured the emission spectra during the afterglow process. The afterglow spectra recorded at 10 s and 1 h after the stoppage of the irradiation are shown in **Figure 4.4**. The profiles of the afterglow emission spectra do not change with time, and only the intensity decreases gradually. This result indicates that the NIR long-persistent luminescence exists in the whole emission spectral region and originates from the Cr^{3+} emitting centers.

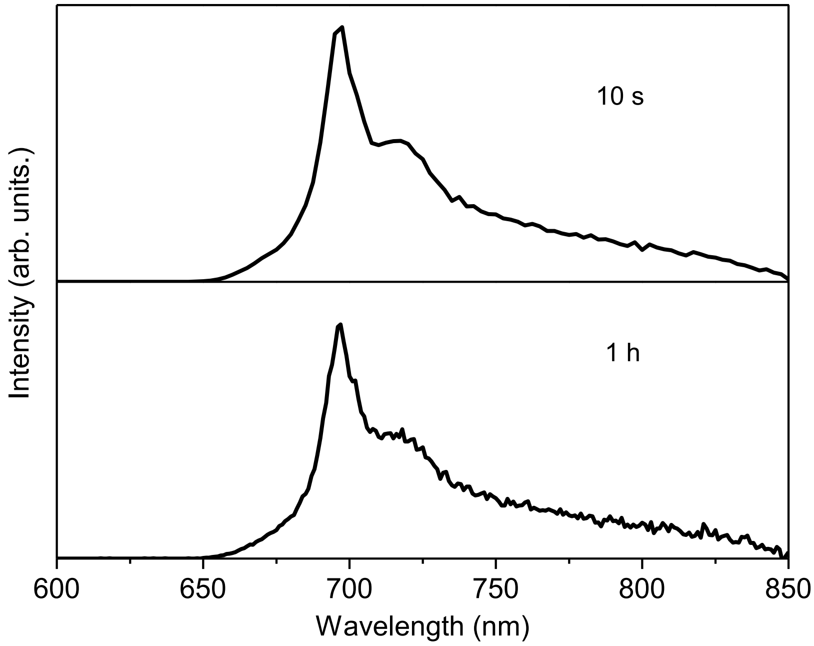

Figure 4.4 Afterglow emission spectra of $Zn_3Ga_2Ge_4O_{14}$:0.1%Cr^{3+} phosphor recorded at 10 s and 1 h after the stoppage of 400 nm irradiation.

The super-long NIR afterglow was also monitored and imaged by a PVS-14 night vision monocular in dark room. **Figure 4.5** shows the NIR photos of twelve $Zn_3Ga_2Ge_4O_{14}$:0.1%Cr^{3+} disks taken by a digital camera via a night vision monocular after exposed to a 365 nm UV lamp for 5 s, 10 s, 30 s, 1min, 5 min and 10 min. The NIR signal can still be detected by the night vision monocular after 348 h continuous NIR emission. **Figure 4.5** clearly shows that the samples can be effectively activated and rapidly charged by UV radiation and that seconds to minutes of UV light irradiation can result in days to weeks (>2 weeks) of persistent NIR light emission. Such very long NIR afterglow indicates that the zinc gallogermanate host has superb capability in absorbing and storing (trapping) the excitation energy and that the storaged energy can then be slowly and efficiently released to Cr^{3+} emitting centers.

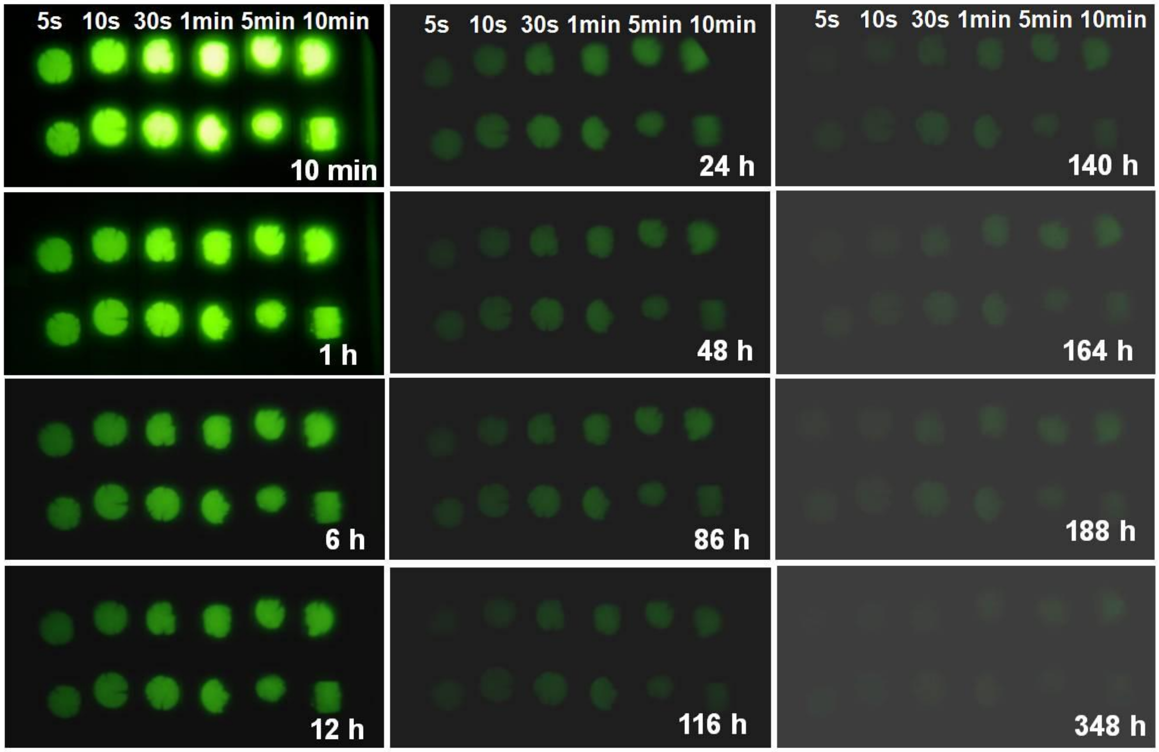

Figure 4.5 NIR afterglow photos of twelve $Zn_3Ga_2Ge_4O_{14}$:0.1%Cr^{3+} disks taken by a digital camera with a night vision monocular after exposed to a 365 nm UV lamp for 5 s, 10 s, 30 s, 1 min, 5 min and 10 min.

The Cr^{3+}-doped zinc gallogermanate phosphors can also be effectively acivated by solar irradiation. **Figure 4.6** shows NIR afterglow photos of eight $Zn_3Ga_2Ge_4O_{14}$:0.1%Cr^{3+} disks taken by a camera via a night vision monocular at different afterglow times (5 min, 22 h, and 138 h) after irradiation with sunlight for 1 min, 5 min 30 min, and 60 min. It is clear that the fading of NIR brigtness corresponding to different exposure times is almost the same, suggesting that $Zn_3Ga_2Ge_4O_{14}$:0.1%Cr^{3+} phosphor has quick charging ability under sunlight.

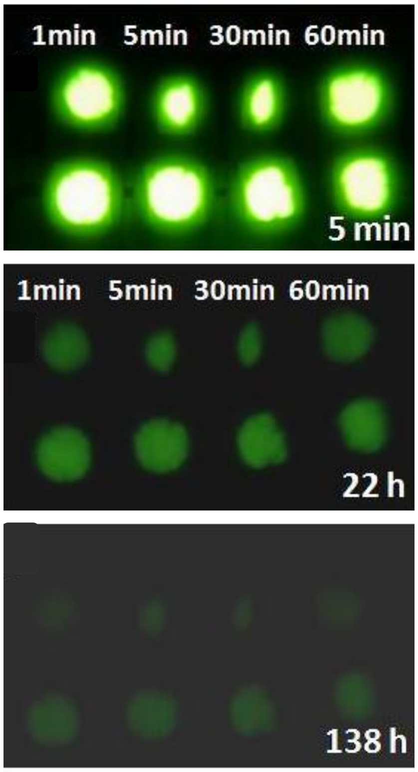

Figure 4.6 NIR afterglow photos of eight $Zn_3Ga_2Ge_4O_{14}$:0.1%Cr^{3+} disks taken by a camera with a night vision monocular at different afterglow times (5 min, 22 h, and 138 h) after irradiation with sunlight for 1 min, 5 min 30 min, and 60 min.

Although the NIR photoluminescence of the Cr^{3+}-doped zinc gallogermanate phosphors can be effectively excited by a wide range of energies (**Figure 4.1**), the situation for the NIR persistent luminescence can be different because of the different activation mechanisms between the photoluminescence and persistent luminescence. To evaluate the effect of different excitation energies on the NIR afterglow, we study the afterglow characteristics of the $Zn_3Ga_2Ge_4O_{14}$:0.1%Cr^{3+} system under the irradiation of a wide range of excitation energies (300 nm to 680 nm) using the Fluorolog-3 spectrofluorometer.

In the evaluation of the excitaiton energy-afterglow relationship, the following two conditions were followed. (1) To avoid the influence of the fast early decay on the analysis of afterglow, the afterglow intensity values at the I_{10s} points under different excitation energies were compared. The point of I_{10s} represents the afterglow intensity recorded at time of 10 s after the stoppage of the irradiation. (2) To all excitation energies, the afterglow was monitored at the same wavelength (696 nm in present study). This is because for the same persistent phosphor, a certain afterglow wavelength is supposed to correpond to particular emitting centers and traps, which allows for fairly evaluating the effectiveness of different excitation energies. **Figure 4.7** shows the afterglow intensity I_{10s} of $Zn_3Ga_2Ge_4O_{14}$:0.1%Cr^{3+} phosphor monitored at 696 nm emission as a function of the excitation wavelengths. Inset in **Figure 4.7** shows the I_{10s} values versus excitation wavelengths from 440 nm to 660 nm for clear vision. **Figure 4.7** clearly shows

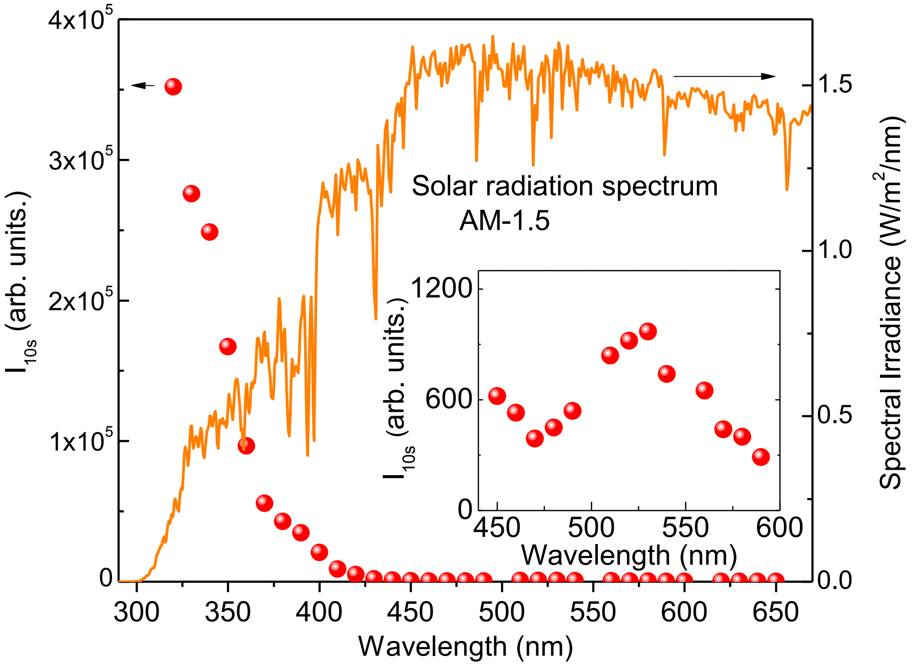

Figure 4.7 Afterglow intensity of $Zn_3Ga_2Ge_4O_{14}$:0.1%Cr^{3+} phosphor monitored at 696 nm emission as a function of the irradiation wavelengths (represented by balls). The solid line curve is the emission spectrum of sunlight under the standard daylight condition (AM 1.5). Inset is I_{10s} values versus excitation wavelengths from 400 nm to 600 nm.

that the NIR afterglow can be effectively achieved under UV illumination (~300-400 nm) but is less effectively achieved under visible light illumination, even though the visible light excitation is very effective to NIR phtoluminescence (see **Figure 4.1**). Note that although the afterglow behaviors at different emission wavelenths may be different in the $Zn_3Ga_2Ge_4O_{14}$:0.1%Cr^{3+} phosphor, the irradiation energy dependences of afterglow intensities monitored at different emission wavelengths, i.e., from 650 nm to 850 nm, show the similar evolutions as that shown in **Figure 4.7**.

The emission spectrum of sunlight under the standard daylight condition (AM 1.5) is also given in **Figure 4.7**. The strong overlap between the energy-afterglow curve and the emission spectrum of the sunlight demonstrates that the NIR long-persistent luminescence from $Zn_3Ga_2Ge_4O_{14}$:0.1%Cr^{3+} can indeed be activated by the solar irradiation.

4.5 Thermoluminescence investigation

Themoluminescence measurement is one of the direct methods to verify the existence of the traps by heating a sample at a linear rate. Traps with one depth correspond to the specific peak temperature and shape in the thermoluminescence spectrum. The fading of the thermoluminescence curves results from the emptying traps, which are governed partially by thermal energy and partially by other processes, such as tunneling or temperature-assisted tunneling [30]. Consequently, thermoluminescence measurements with different delay times after ceasing irradiation could be employed to distinguish the traps.

To learn the distribution of the traps in Cr^{3+}-doped zinc gallogermanate phosphors, thermoluminescence measurements with different delay times were conducted. **Figure 4.8** shows the thermoluminescence curves of $Zn_3Ga_2Ge_4O_{14}$:0.1%Cr^{3+} phosphor monitored at 696 nm with delay times of 10 s and 2 h after ceasing irradiation with a Xe lamp at 320 nm for 10 min. The thermoluminescence curve measured at 10 s after irradiation shows an asymmetric broadband, covering the 30 to 300 °C temperature range. Such an asymmetric broadband implies the existence of overlapping components. As the delay time increases to 2 h, the low-temperature band at ~60 °C vanishes, and the high-temperature band (~30 °C to ~300 °C) still exists. In a comparison of the two given thermoluminescence curves, we can see that the fading rate of the high-temperature band peaked at ~110 °C is rather slow and thus is mainly responsible for the long afterglow of the persistent NIR luminescence. Therefore, with different delay times, two overlapping components can be distinguished: low-temperature and high-temperature band.

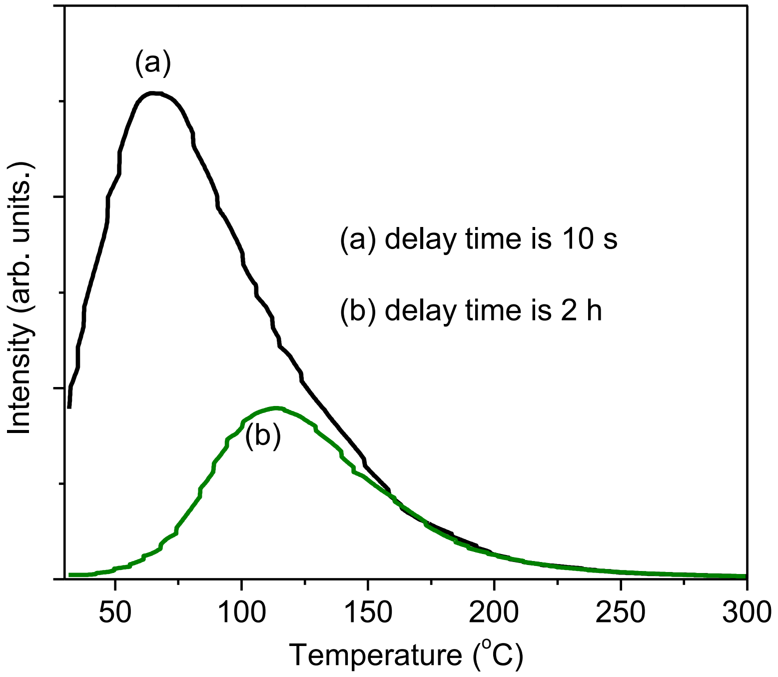

Figure 4.8 Thermoluminescence curves of $Zn_3Ga_2Ge_4O_{14}$:0.1%Cr^{3+} phosphor monitored at 696 nm with delay times of 10 s and 2 h after ceasing the irradiation of a Xenon lamp (at 320 nm for 10 min).

Figure 4.9 shows the thermoluminescence curves of $Zn_3Ga_2Ge_4O_{14}$:0.1%Cr^{3+} phosphor monitored at 696 nm with irradiation at 360 nm and 400 nm, (from the Xe lamp) for 5 min. The area under the thermoluminescence curve is proportional to the total number of trapped charge carriers. Therefore, the traps are filled more effective under irradiation at 360 nm than at 400 nm. This result is consistent with the excitation energy-afterglow relationship measurement shown in **Figure 4.7**.

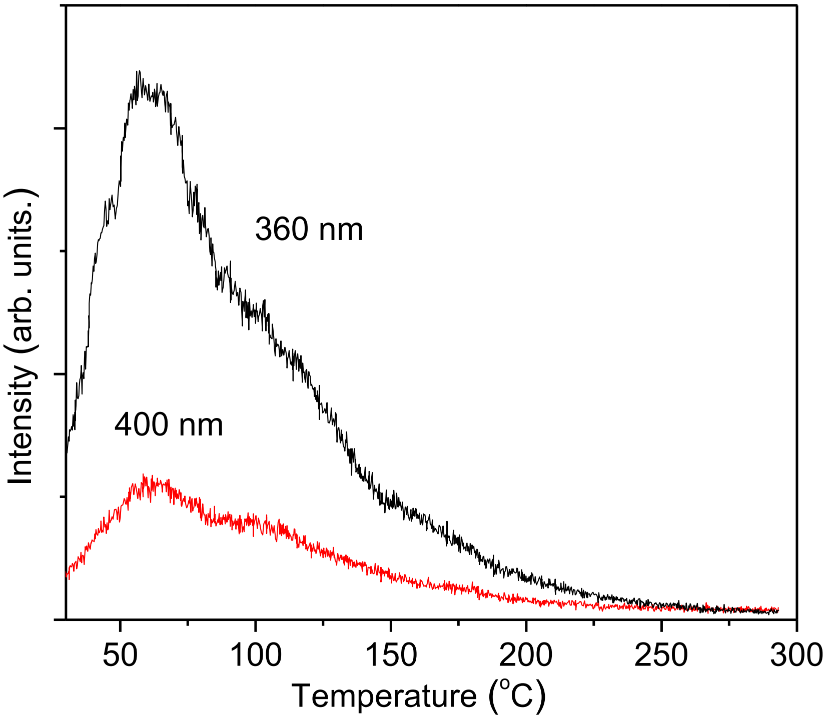

Figure 4.9 Thermoluminescence curves of $Zn_3Ga_2Ge_4O_{14}$:0.1%Cr^{3+} phosphor monitored at 696 nm after irradiation at 360 nm and 400 nm for 5 min.

4.6 Long-persistent luminescence mechanism

Up to now, the exhaustive process governing long-perststent luminescnece is not clear, even for the well-studied visible long-persistent phosphors. This is because that the identification of the origin and nature of defects are not easy. Moreover, there is still no reliable method to locate the ground states of dopants relative to conduction band at the present stage. Here, we give a preliminary discussion based on the reported results.

For the decay of a persistent phosphor, if the persistent luminescence intensity (I)-decay time (*t*) curve can be fitted by $I \propto t^{-n}$ where $0.5 \le n \le 1$, a tunneling-related process is usually involved in the persistent luminescence[64,65,89]. **Figure 4.10** shows the log-log plot of the *I-t* curve of $Zn_3Ga_2Ge_4O_{14}$:0.1%Cr^{3+} phosphor. The *I-t* curve can be fitted by a curve of $I = 2.5\times 10^8 t^{-0.98}$, as represented by the red line in **Figure 4.10**. Ther perfect fitting therefore indicates that the detrapping process of persistent luminescence in the $Zn_3Ga_2Ge_4O_{14}$:0.1%Cr^{3+} phosphor possibly occurs through a tunneling or temperature–assisted tunneling process.

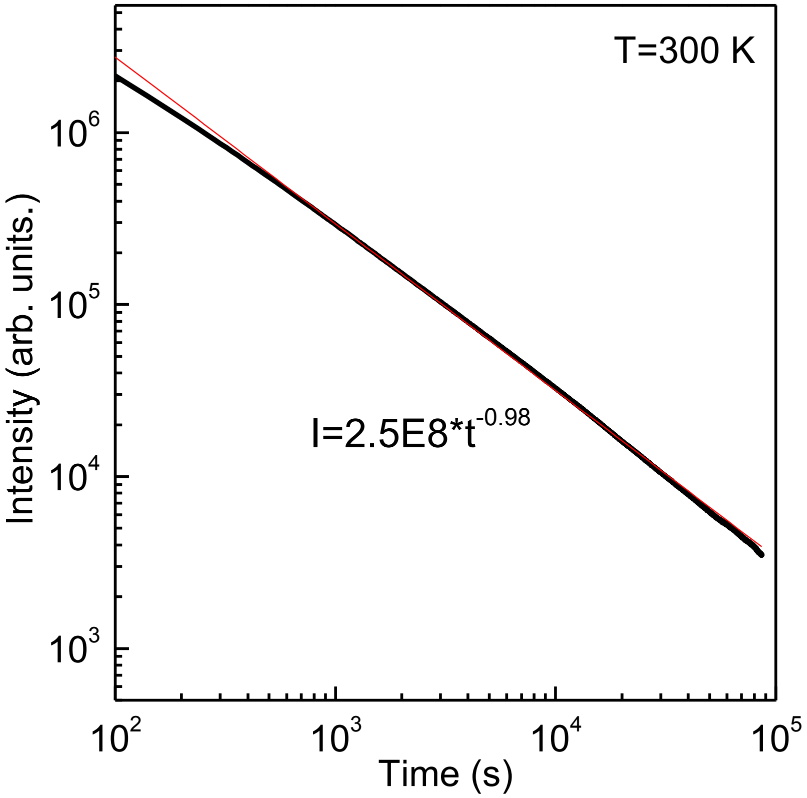

Figure 4.10 Fitting of persistent luminescence decay of $Zn_3Ga_2Ge_4O_{14}$:0.1%Cr^{3+} phosphor at room temperature. The phosphor was excited by a 365 nm UV lamp for 10 min. The decay curve was monitored at 696 nm.

We also measured the afterglow decay curve monitored at 696 nm at 77 K, as shown in **Figure 4.11**. Before the afterglow decay curve measurements, the sample was irradiated with the

Xe lamp at 320 nm for 5 min. The afterglow decay curve at 77 K also satisfies the equation of $I = I_0 \times t^{-n}$, where n = 0.55, I_0 = 5500, which further supports the participation of tunneling process. The variation in afterglow decay rates with temperature can be ascribed to the involvement of thermal-assisted tunneling recombination. Based on the results of the afterglow decay curves and the thermoluminescence measurements, a possible mechanism was proposed, as shown in **Figure 4.12**. Initially, Cr^{3+} ions are excited under external irradiation. Part of the excited electrons of Cr^{3+} ions can be captured by the traps, and Cr^{4+} ions are left behind as a result. With the assumption of a tunneling mechanism, traps must be in the vicinity of Cr^{3+} ions.

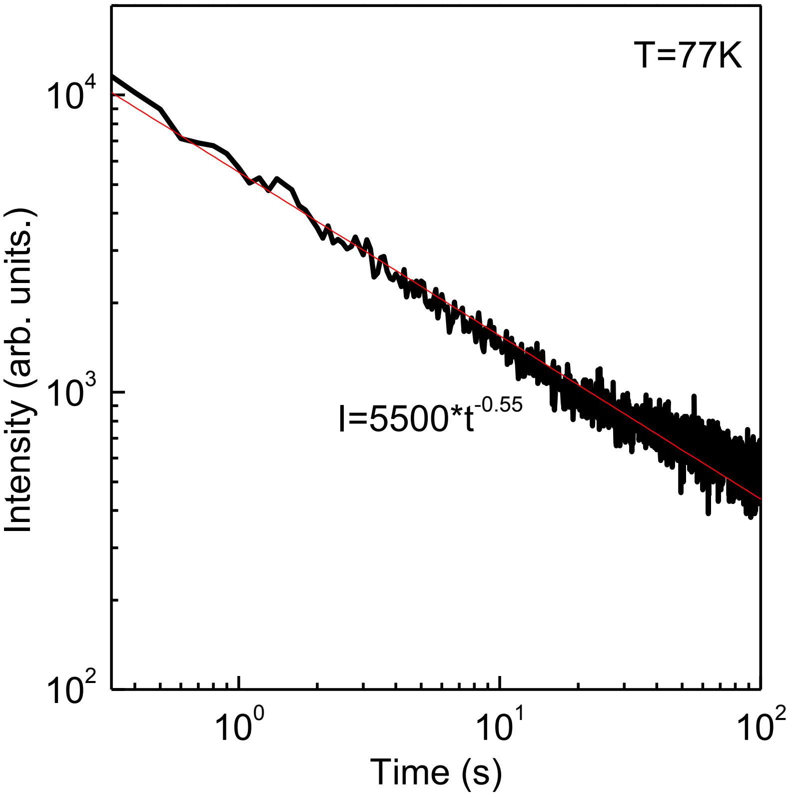

Figure 4.11 Afterglow decay curve of $Zn_3Ga_2Ge_4O_{14}$:0.1%Cr^{3+} phosphor monitored at 696 nm at 77 k after exposed to 320 nm Xenon lamp for 5 min.

When the trapped electrons tunnel through the barrier and continuously recombine with photo-generated Cr^{4+}, persistent Cr^{3+} emission occurs.

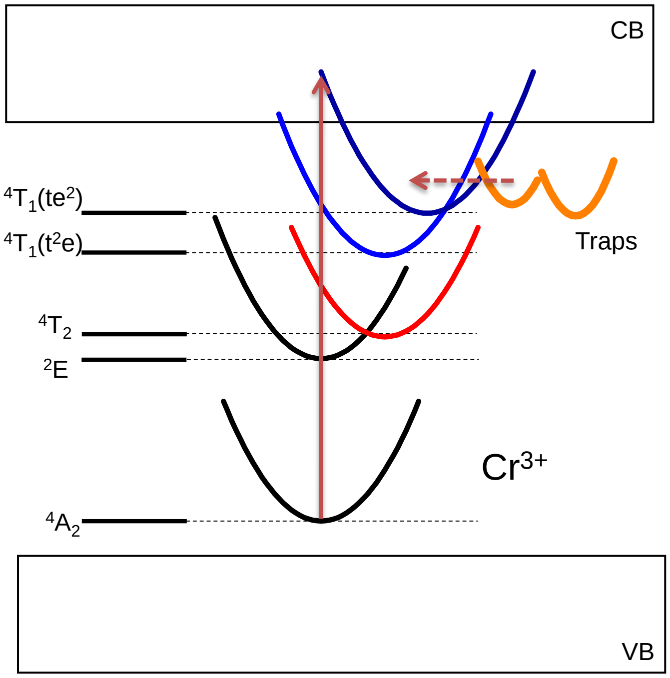

Figure 4.12 Schematic diagram of the persistent NIR luminescence of $Zn_3Ga_2Ge_4O_{14}$:0.1%Cr^{3+} phosphor. The straight line arrows and dashed line arrow represent the optical transitions and electron transfer process respectively.

4.7 Persistent luminescence activated by solar radiation

In **Figure 4.6** and **Figure 4.7** we have shown that the Cr^{3+}-doped zinc gallogermanates can be efficiently activated and quickly charged by the sunlight and give persistent luminescence as long and efficient as the cases under UV light illumination. Our extensive outdoor experiments further show that our materials can be effectively activated by solar radiation at any weather conditions (sunny, cloudy and rainy day), at any moment between sunrise and sunset, at any outdoor locations (open area and the shadows of the trees and buildings), and in various aqueous medium (tap water, salt water, and bleach-containing aqueous solution). These mean that the Cr^{3+}-doped zinc gallogermanates have very high response to not only direct sunray but also diffuse light of the solar radiation. **Figure 4.13** shows the afterglow decay curves of $Zn_3Ga_2Ge_4O_{14}$:0.1%Cr^{3+} disks activated by solar radiation for 5 min in a sunny day, a cloudy day and a rainy day. The decay curves were acquired by the Fluorolog-3 spectrofluorometer two minutes after the activation (it needs two minutes to take the samples back to the spectrofluorometer chamber for decay measurements). The decay curves of the samples activated in different weather conditions exhibit similar decay tendency, indicating that the samples can be effectively activated by both direct sunray (in sunny day) and diffuse light (in cloudy or rainy day).

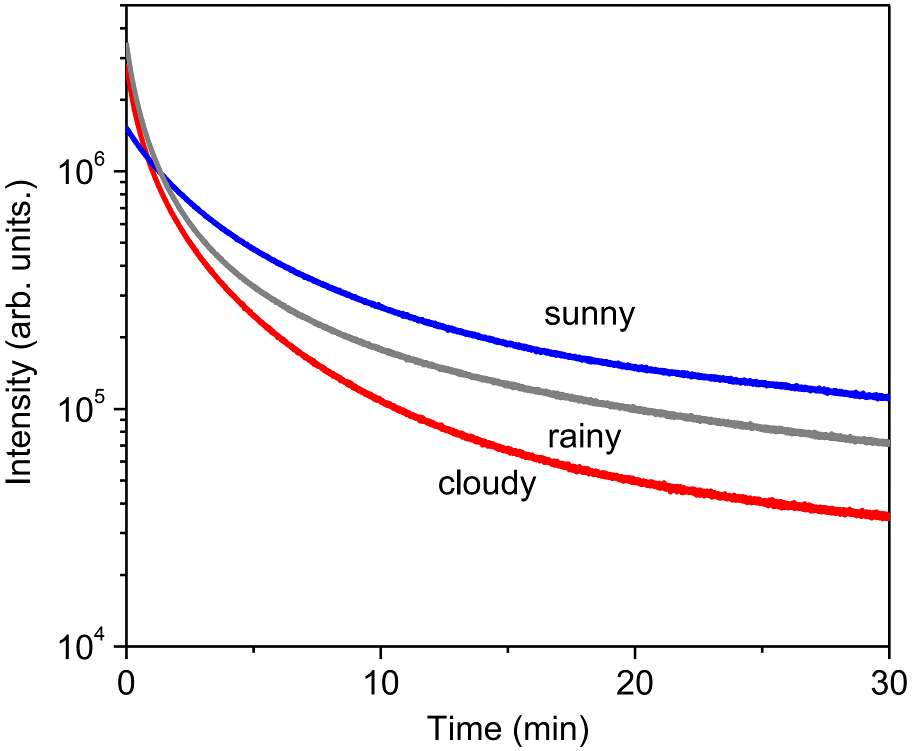

Figure 4.13 Afterglow decay curves of $Zn_3Ga_2Ge_4O_{14}$:0.1%Cr^{3+} activated by solar radiation for 5 min in a sunny day, a cloudy day and a rainy day.

The effectiveness of the diffuse light on the activation and charging of the Cr^{3+}-doped zinc gallogermanates was further verified by exciting the samples in the shadows of trees or buildings. **Figure 4.14** shows the afterglow images of two $Zn_3Ga_2Ge_4O_{14}$:0.1%Cr^{3+} disks after exposed in the shadow of a building for 5 min. By comparing with the images shown in **Figure 4.6** where the samples were activated by direct sunray, it can be found that the excitation by the diffuse light is as effective as that by the direct sunray.

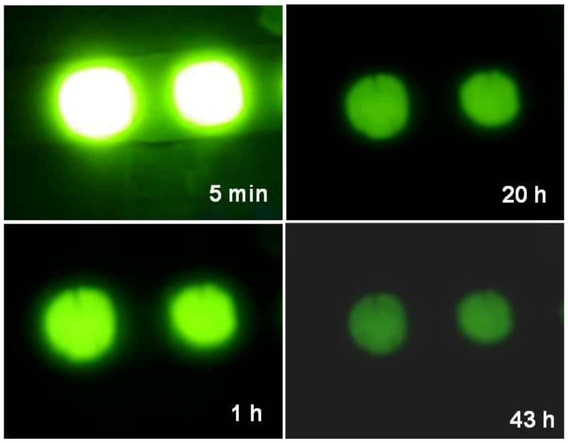

Figure 4.14 NIR afterglow photos of two $Zn_3Ga_2Ge_4O_{14}$:0.1%Cr^{3+} disks after exposed in the shadow of a building for 5 min. The photos were taken by a digital camera with a night vision monocular.

Besides the activation in air, the Cr^{3+}-doped zinc gallogermanates can also be effectively activated by solar radiation in various aqueous solutions including tap water, salt water (the same NaCl concentration as the sea water), and more corrosive NaCl-$NaHCO_3$-bleach aqueous solution, and the materials exhibit extraordinary stability in these solutions. **Figure 4.15** shows the afterglow images of two $Zn_3Ga_2Ge_4O_{14}$:0.1%Cr^{3+} disks immersed in salt water after exposed in sunlight for 5 min. After 100 h of persistent luminescence, the disks can still be clearly seen by the night vision monocular. The afterglow decay curve of the $Zn_3Ga_2Ge_4O_{14}$:0.1%Cr^{3+} disk excited in tap water by sunlight is shown in **Figure 4.16**. For comparison, the afterglow decay curve of the same disk excited in air by sunlight is also displayed. Even though there exists difference in absolute emission intensity, the samples in water and air show similar decay tendency.

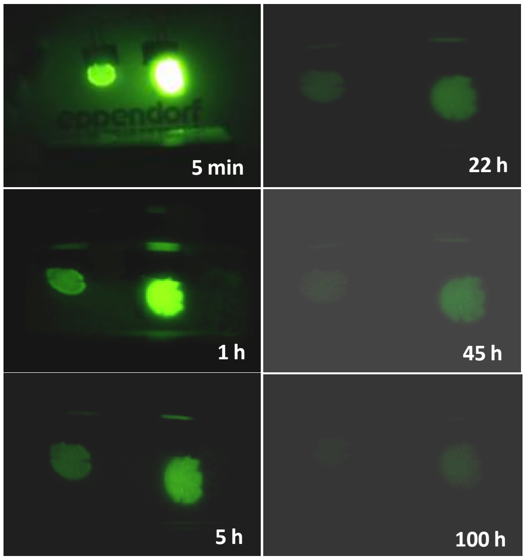

Figure 4.15 NIR afterglow photos of two $Zn_3Ga_2Ge_4O_{14}$:0.1%Cr^{3+} disks immersed in salt water after exposed in sunlight for 5 min. The photos were taken by a digital camera with a night vision monocular.

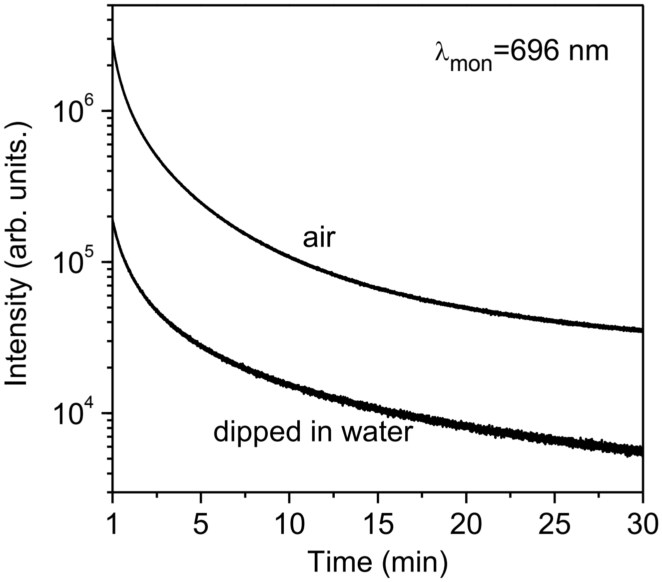

Figure 4.16 Afterglow decay curves of $Zn_3Ga_2Ge_4O_{14}$:0.1%Cr^{3+} phosphor excited in tap water and in air by sunlight. The monitored wavelength is 696 nm.

Figure 4.17 shows that the $Zn_3Ga_2Ge_4O_{14}$:0.1%Cr^{3+} phosphor disks can be effectively activated by solar radiation when they were immersed in a corrosive NaCl-$NaHCO_3$-bleach aqueous solution. The aqueous solution was made by adding 20 drops of bleach, 5 grams of NaCl and 3 grams of $NaHCO_3$ into 75 ml tap water. To keep the solution in a basic pHs and oxidizing conditions, every week 20 drops of bleach and 1 gram of $NaHCO_3$ were added to compensate the evaporation loss. Every week, the samples together with the solution were taken out for recharging by sunlight for 5 minutes and then taken back to the dark room for imaging using the night vision monocular. The number at the bottom right corner of each image is the days that the samples were immersed in the solution. **Figure 4.17** clearly show that the samples immersed in the solution for 15 weeks exhibit the same excitation, emission, and persistence performance as the fresh ones. No apparent corrosion was observed after 100 days of immersion in the NaCl-bleach-$NaHCO_3$ aqueous solution.

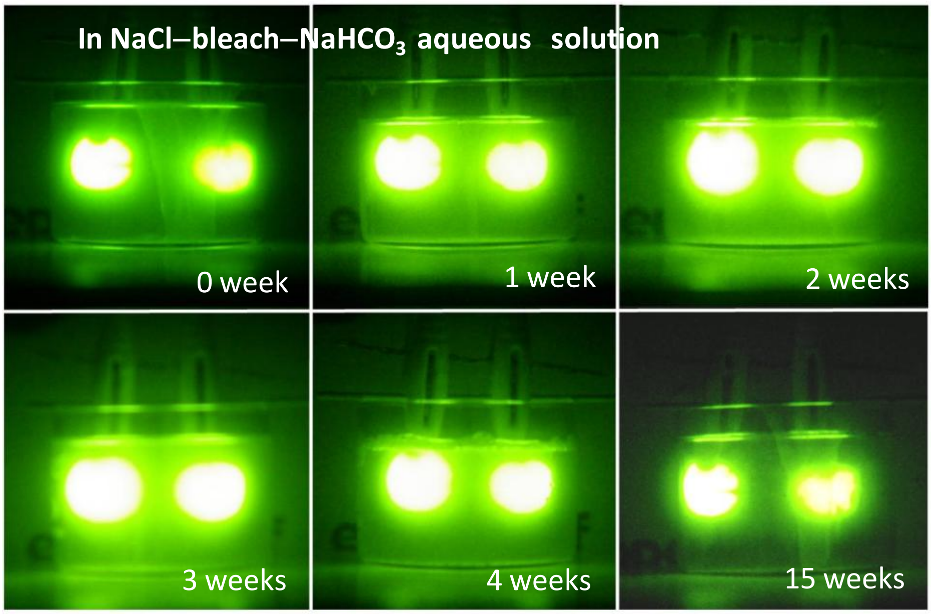

Figure 4.17 NIR afterglow photos of two $Zn_3Ga_2Ge_4O_{14}$: 0.1% Cr^{3+} disks immersed in a NaCl-bleach-bicarbonate ($NaHCO_3$) aqueous solution after exposed in sunlight for 5 min. The photos were taken by a digital camera with a night vision monocular.

The above results (**Figures 4.5, 4.6, 4.14, 4.15** and **4.17**) have shown that the Cr^{3+}-doped zinc gallogermanate disks emit intense NIR light after short excitation by UV light or sunlight. Such intense NIR emission can be used as secret (invisible to unaided eyes) lighting source for reading in the dark, as that shown in **Figure 4.18**. The disks were activated by sunlight for 5 minutes. The content on the paper was printed by a laser printer.

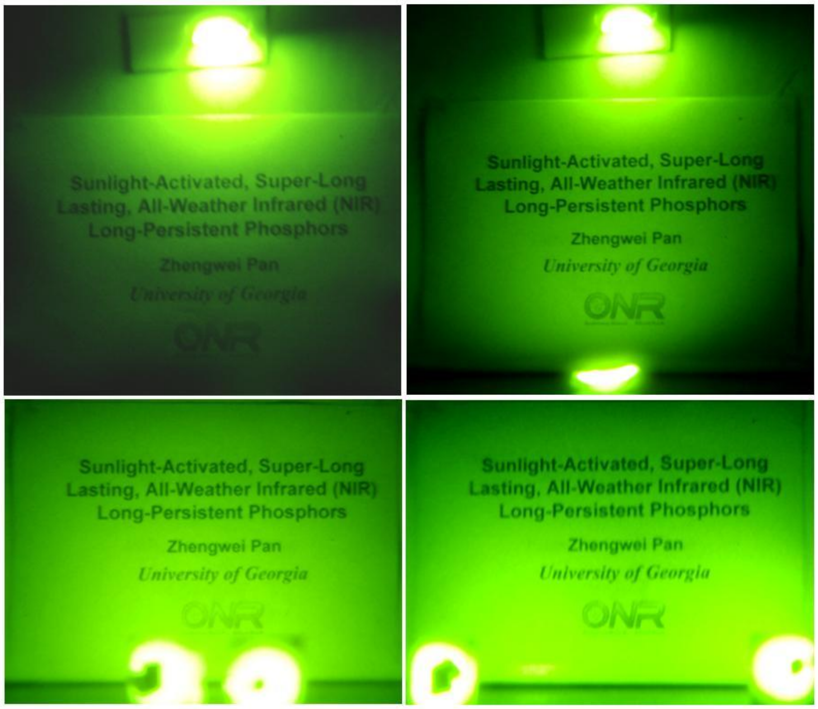

Figure 4.18 NIR afterglow photos of sunlight-activated $Zn_3Ga_2Ge_4O_{14}$: 0.1%Cr^{3+} disks used as efficient, secret lighting sources in the dark. The photos were taken by a digital camera with a night vision monocular.

4.8 Cr^{3+}-doped zinc gallogermanate NIR persistent luminescent paints

The powder form of the Cr^{3+}-doped zinc gallogermanate phosphors can be incorporated into various water-based and oil-based paints to form NIR luminescent paints or inks. This can endow the paints or inks emitting NIR light after excitation by either UV light or sunlight. The water-based paints are preferably regular indoor-used wall paints. The oil-based paints are mainly transparent or colorless resins and vanish. The preferred resins include epoxy resin, polyurethane resin, polyester resin, acrylic acid resin, and hydroxyl acrylic acid resin. The preferred vanish includes amino varnish, acrylic polyurethane coating, and transparent alkyd coating. To prepare the NIR paints, the quantity of the phosphor powder added to the paints is typically about 10 wt. % to 50 wt. %. **Figure 4.19** shows the NIR images of the logos of the University of Georgia (UGA) and the office of Naval Research (ONR) written with the paint made from the $Zn_3Ga_2Ge_4O_{14}$:0.1%Cr^{3+}.

Figure 4.19 NIR afterglow photos of the logos of the University of Georgia (UGA) and the Office of Naval Research (ONR) written with the paint made from $Zn_3Ga_2Ge_4O_{14}$:0.1%Cr^{3+} phosphor powders with acrylic polyurethane varnish. The photos were taken by a digital camera with a night vision monocular. The quantity of the phosphor powders in the varnish is 30 wt. %. The logos were exposed to sunlight for 5 minutes. The logos can be clearly seen after 100 h with the night vision monocular.

4.9 Influences of cr^{3+} concentrations and host compositions on the optical properties of the phosphors

As that mentioned in Section 4.2, remarkable NIR persistent luminescence can be achieved over a wide range of Cr^{3+} concentrations and host compositions. In the previous sections, we focused our discussions on $Zn_3Ga_2Ge_4O_{14}$:0.1%Cr^{3+} phosphor. In this section, we will briefly discuss the phosphors with Cr^{3+} concentrations at 0.5 mol% and 1 mol%, and the phosphors in which Ga and Ge ions are, respectively, partially or fully replaced by other IIIA and IV ions.

Figure 4.20 shows the normalized excitation and emission spectra (blue solid line curves) of $Zn_3Ga_2Ge_4O_{14}$:1%Cr^{3+} phosphor. For comparison, the normalized excitation and emission spectra (red dashed line curves) of $Zn_3Ga_2Ge_4O_{14}$:0.1%Cr^{3+} phosphor were also displayed in **Figure 4.20** (it originally displayed in **Figure 4.1**). It is clear that the excitation and emission spectra of the $Zn_3Ga_2Ge_4O_{14}$ phosphors vary with the Cr^{3+} ion concentration. When the

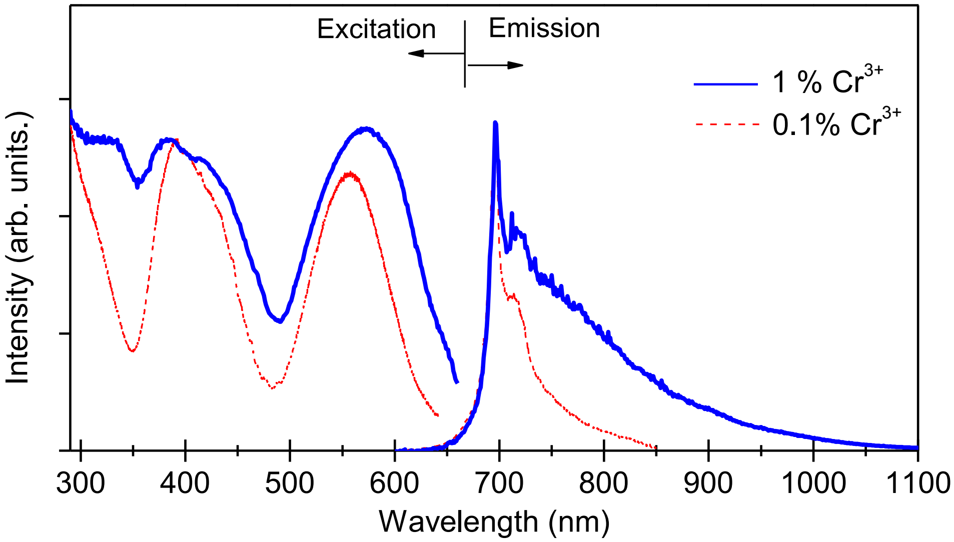

Figure 4.20 Normalized excitation and emission spectra (solid line curves) of $Zn_3Ga_2Ge_4O_{14}$:1%Cr^{3+} phosphor. The dot line curves are the normalized excitation and emission spectra of $Zn_3Ga_2Ge_4O_{14}$:0.1%Cr^{3+} phosphor.

Cr^{3+} concentration increases from 0.1% to 1%, the excitation becomes more effective and the broad emission band due to the $^4A_2 \rightarrow ^4T_1$ transitions becomes more significant. The emission spectrum of the $Zn_3Ga_2Ge_4O_{14}$:1%Cr^{3+} sample expands to ~1100 nm.

Figure 4.21 shows the decay curves of $Zn_3Ga_2Ge_4O_{14}$:0.1%Cr^{3+}, $Zn_3Ga_2Ge_4O_{14}$:0.5%Cr^{3+} and $Zn_3Ga_2Ge_4O_{14}$:1%Cr^{3+} phosphors monitored at 696 nm after irradiation with a 365 nm UV lamp for 10 min. All the three phosphors exhibit remarkable persistent luminescence performance with the 1 mol% Cr^{3+} sample having relatively shorter duration time. This is understandable when considering the amount of emitting centers. The 1 mol% Cr^{3+} sample have much more Cr^{3+} emitting centers compared with the 0.5 mol% Cr^{3+} and 0.1 mol% Cr^{3+} samples, which results in quicker release of the trapped charge carriers.

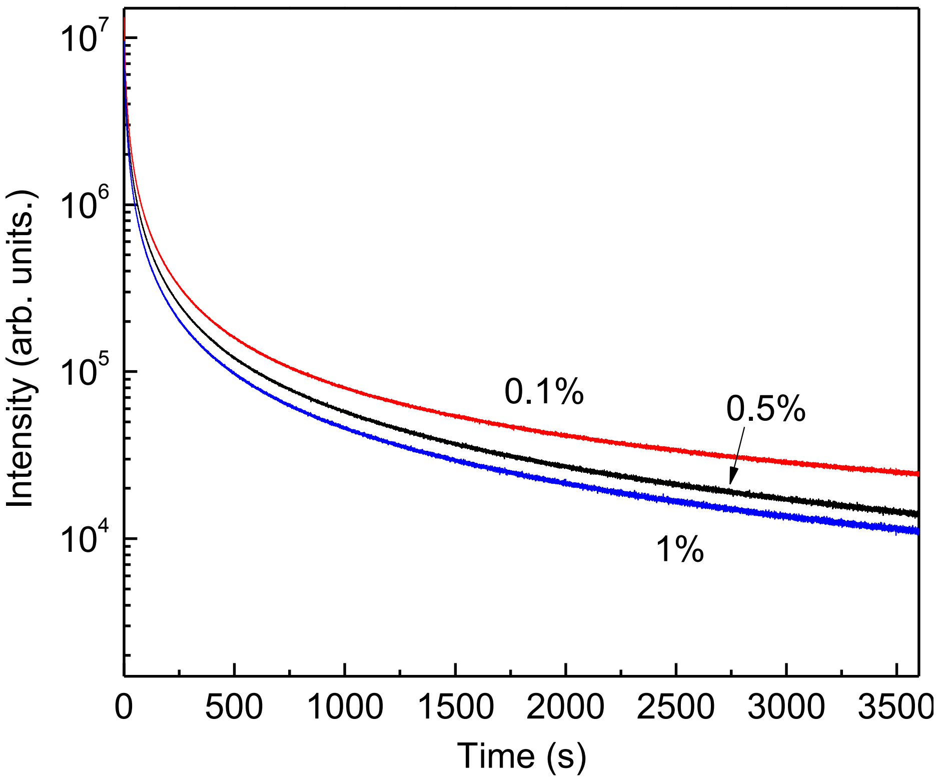

Figure 4.21 Afterglow decay curves of $Zn_3Ga_2Ge_4O_{14}$:0.1%Cr^{3+}, $Zn_3Ga_2Ge_4O_{14}$:0.5%Cr^{3+}, and $Zn_3Ga_2Ge_4O_{14}$:1%Cr^{3+} monitored at 696 nm after irradiation with a 365 nm UV lamp for 10 min.

We also adjusted the compositions of the hosts by partially or fully substituting In^{3+} ions for Ga^{3+} ions or Sn^{4+} ions for Ge^{4+} ions. **Figure 4.22a**, **b**, and **c** show the normalized excitation and emission spectra of the $Zn_3(GaIn)Ge_4O_{14}$:0.1%Cr^{3+}, $Zn_3Ga_2(Ge_2Sn_2)O_{14}$:0.1%Cr^{3+}, and $Zn_2Ga_2Sn_4O_{14}$:0.1%Cr^{3+} phosphors, respectively. The afterglow decay curves of these three

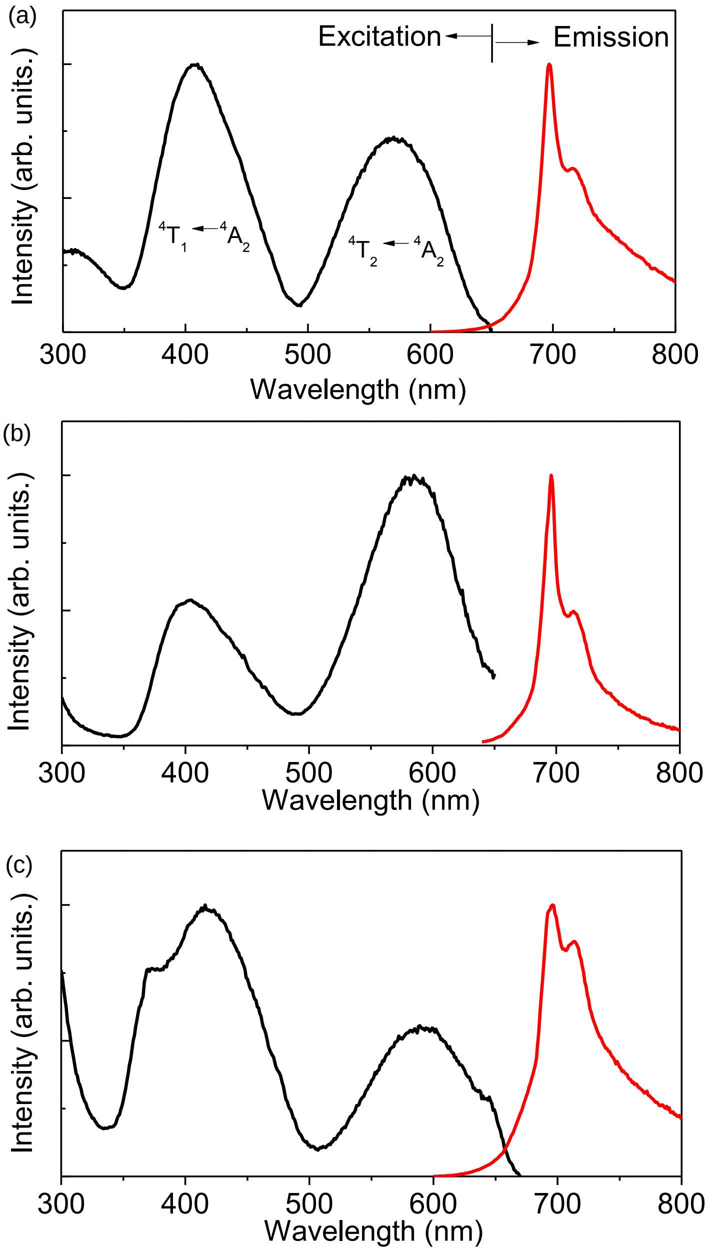

Figure 4.22 Normalized excitation and emission spectra of (a) $Zn_3(GaIn)Ge_4O_{14}$:0.1%Cr^{3+}, (b) $Zn_3Ga_2(Ge_2Sn_2)O_{14}$: 0.1%Cr^{3+} , and (c) $Zn_3Ga_2Sn_4O_{14}$:0.1%Cr^{3+} phosphors.

phosphors under solar radiation in sunny day are shown in **Figure 4.23**. By comparing with the excitation and emission spectra in **Figure 4.1** and the afterglow decay curve in **Figure 4.3**, both related to $Zn_3Ga_2Ge_4O_{14}$:0.1%Cr^{3+} phosphors, it can be found that using In^{3+} ions to partially replace Ga^{3+} ions or using Sn^{4+} ions to partially or fully replace Ge^{4+} ions in the hosts do not significantly alter the photoluminescence and afterglow properties of the phosphors. These results suggest that the hosts that are suitable for Cr^{3+} NIR persistent emission can be far beyond the zinc-gallium-germanium systems.

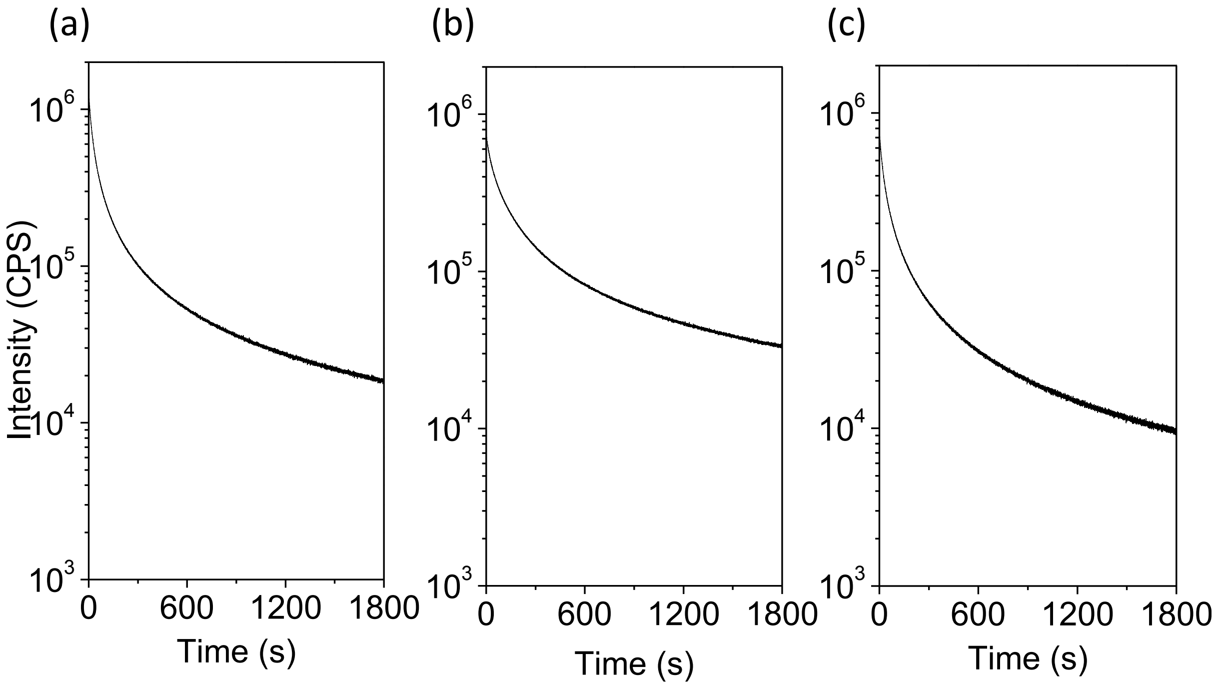

Figure 4.23 Afterglow decay curves of (a) $Zn_3(GaIn)Ge_4O_{14}$:0.1%Cr^{3+}, (b) $Zn_3Ga_2(Ge_2Sn_2)O_{14}$:0.1%Cr^{3+}, and (c) $Zn_3Ga_2Sn_4O_{14}$:0.1%Cr^{3+} phosphors monitored at 696 nm.

4.10 Summary

We have developed a novel series of Cr^{3+}-doped zinc gallogermanate NIR persistent phosphors. These phosphors exhibit extraordinary capabilities in excitation energy absorption, storage, NIR light conversion, and persistent NIR luminescence. Seconds to minutes of UV or sunlight activation can result in days to weeks (>2 weeks) of continuous NIR persistent luminescence. Especially, the Cr^{3+}-doped zinc gallogermanates can be effectively activated by solar radiation at any weather conditions (sunny, cloudy and rainy day), at any moment between sunrise and sunset, at any outdoor locations (open area and the shadows of the trees and buildings), and in various aqueous medium (tap water, salt water, and bleach-containing aqueous solution). Detailed investigations reveal that the detrapping process is governed by tunneling and thermal-assisted tunneling recombination mechanisms. The super-long lasting NIR afterglow, the ability to be repeatedly activated and charged by solar radiation, the extraordinary capability in storing solar energy, and the outstanding chemical stability suggest that the the Cr^{3+}-doped zinc gallogermanates can find important applications in many important areas including as identification taggants to tag, track and locate targets of interests in denfense and security, as solar energy absorber and converter in solar energy utilization and in achieving high-efficiency photovoltaics, and as optical probes in *in vivo* deep tissue bio-imaging.

CHAPTER 5

CONCLUSIONS AND OUTLOOK

In this dissertation, we have discovered and developed two novel series of Cr^{3+}-activated gallate-based NIR persistent phosphors: Cr^{3+}-doped β-Ga_2O_3 nanowires with persistence time more than 4 h and Cr^{3+}-doped zinc gallogermanates with persistence time more than 400 h. Our results have shown that gallates, especially zinc- and germanium-incorporated gallates (i.e., zinc gallogermanates) are very suitable hosts for persistent NIR emission from Cr^{3+} ions by creating appropriate traps and efficiently releasing the trapped electrons and holes to the Cr^{3+} emitting centers. Our research thus opens a new avenue for NIR persistent phosphors that are new but have very promising applications in security and defense, solar energy utilization, and *in vivo* deep-tissue bio-imaging.

Cr^{3+}-doped β-Ga_2O_3 nanowires: The Cr^{3+}-doped β-Ga_2O_3 nanowires were synthesized by hydrothermal reaction of $GaCl_3$ and $Cr(NO_3)_3$ at 180 °C for 24 h followed by calcinations at 900 °C in air for 2 h. The presence of Ca^{2+} ions in the solution can tune the diameter and length of the nanowires but does not alter the nanowires' optical performance.

The NIR luminescence of the β-Ga_2O_3:Cr^{3+} nanowires can be effectively activated by a broad range of wavelengths ranging from ~250 nm to ~650 nm. The emission exhibits characteristic emission from Cr^{3+} ions, featuring a broadening R line at 696 nm (attributed to $^2E \rightarrow {}^4A_2$ transition of Cr^{3+}) superimposing on a broad emission band (650–850 nm; attributed to $^4T_2 \rightarrow {}^4A_2$ transition of Cr^{3+}) peaked at 711 nm. The coexistence of the R line and the broad emission band in the emission spectrum suggests that the Cr^{3+} ions substitute Ga^{3+} ions in the distorted octahedral sites of the Ga_2O_3 host and experience intermediate crystal field strength.

Even thought the NIR luminescence of the β-Ga_2O_3:Cr^{3+} nanowires can be effectively activated by wavelengths ranging from ~250 nm to ~650 nm, the NIR persistent luminescence can only be induced by UV lights in the wavelength range of ~250–370 nm. After irradiation with a 254 nm UV lamp for 5 minutes, the NIR afterglow can last for more than 4 h. The profiles of the afterglow spectra do not change with decay periods, indicating that the NIR persistent luminescence exists in the whole emission spectral region and originates from the Cr^{3+} emitting centers.

Thermoluminescence measurements on the β-Ga_2O_3:Cr^{3+} nanowires reveals the existence of at least two traps with different trapping depths: low-temperature (~50 ℃ to ~250 ℃) shallow trap and high-temperature (25 ℃ to ~100 ℃) deep trap, with the latter one being mainly responsible for the long afterglow of the persistent NIR luminescence.

Cr^{3+}-doped zinc gallogermanate powders and ceramics: The Cr^{3+}-doped zinc gallogermanates were synthesized by solid-state reaction of ZnO, Ga_2O_3, GeO_2 and Cr_2O_3 powders at ~900 °C for prefiring and ~1100–1250 °C for sintering. Remarkable NIR persistent luminescence was achieved over a broad host compositions and Cr^{3+} ion concentration. The general chemical formula of the Cr^{3+}-doped zinc gallogermanates can be written as $Zn_xGa_yGe_zO_{(x+(3y/2)+2z)}$:$tCr^{3+}$, mR, where R is a co-dopant selected from a group consisting ofalkaline earth ions, lanthanide ions, and Li^+ ions; x, y, and z are integers from 1 to 5; t is 0.01 mol% to 2 mol% based on the total moles of Ga; and m is 0 to 2 mol% based on the total moles of Ga. In this dissertation, we used $Zn_3Ga_2Ge_4O_{14}$:0.1%Cr^{3+} as an example to demonstrate the superb capabilities of the Cr^{3+}-doped zinc gallogermanates in excitation energy absorption, storage, NIR light conversion, and NIR light persistent luminescence.

The Cr^{3+}-doped zinc gallogermanates can be effectively activated by a wide range of wavelengths ranging from ~300 nm to ~650 nm, and emit intense, broad NIR light (under excitation) and very long NIR afterglow (after stoppage of excitation). The luminescence emission spectra and afterglow emission spectra have the same profile and are characteristic emission from Cr^{3+} ions, which features a broadening R line at 696 nm (attributed to $^2E \rightarrow {}^4A_2$ transition of Cr^{3+}) superimposing on a broad emission band (700–1100 nm). The persistent luminescence of the Cr^{3+}-doped zinc gallogermanates lasts for more than 400 h, which is about two orders of magnitude longer than that achieved previously.

Due to the strong overlap between the phosphors' excitation spectrum and the solar radiation spectrum received on Earth, the Cr^{3+}-doped zinc gallogermanates exhibit extraordinary capabilities in solar energy absorption and storage. Specifically, the Cr^{3+}-doped zinc gallogermanates can be effectively activated and rapidly charged by solar radiation in various outdoor environments, including (1) in any weathering conditions (sunny, cloudy and rainy days), (2) at any moments between sunrise and sunset, (3) in any outdoor locations (e.g., open area and shadows of trees and buildings), and (4) in various aqueous solutions (e.g., rain water, salt water, and $NaCl$-$NaHCO_3$-bleach aqueous solution). Seconds to minutes of solar radiation activation can result in days to weeks (>2 weeks) of NIR persistent luminescence. The outdoor measurements revealed that the Cr^{3+}-doped zinc gallogermanates have very high response to not only direct sunray but also diffuse light of the solar radiation.

The Cr^{3+}-doped zinc gallogermanates can be prepared in the forms of powders and ceramics. The powders can be incorporated into water-based or oil-based paints to form NIR persistent paints or inks. This endows the paints or inks emitting persistent NIR light after excitation by either UV light or sunlight.

Based on the afterglow decay tendency and thermoluminescence measurements, our theoretical investigations suggest that the detrapping process in the Cr^{3+}-doped zinc gallogermanates is governed by tunneling and thermal-assisted tunneling recombination mechanisms.

The ability to be effectively activated and rapidly charged by solar radiation, the intense and broad NIR emission, as well as the super-long lasting NIR afterglow, make the Cr^{3+}-doped zinc gallogermanates have very promising applications in many important areas. For examples, the phosphors (1) can be used as taggants to tag, track and locate (TTL) targets of interests in security, defense and forensics; (2) can be used to absorb and store solar energy; (3) can be used as converter to convert high-energy solar photons (UV-blue-green) to low-energy NIR photons that can be efficiently absorbed by Si solar cells and thus increase the Si cells' efficiency; and (4) can be used as optical probes for *in vivo* deep-tissue bio-imaging.

Outlook: In this dissertation, we have showed that long-lasting NIR persistent luminescence can be realized by using gallates as hosts and Cr^{3+} ions as emitting centers. Especially, Cr^{3+}-doped zinc gallogermanates exhibit extraordinary capability in solar energy absorption, storage, NIR light conversion, and very long NIR afterglow. While the materials are novel and promising, however, there are many fundamental questions remained to be answered, especially regarding to the Cr^{3+}-doped zinc gallogermanates. These include, but are not limited to:

(1) How do the compositions, concentrations, and processing conditions affect the optical properties of the phosphors? Can we find more efficient host systems? Can we find other emitting centers so that to expand the emission wavelengths to well beyond 1000 nm?

(2) Why can the materials absorb the (solar) energy so effectively and rapidly? What are the trapping mechanisms for electrons and holes? How about the states of the traps (density, distribution and depth) in the host?

(3) Why can the materials have so high capacity to store the energy?

(4) Why can the stored electrons and holes be released so slowly (>100 h)? What are the detrapping and transferring mechanisms?

(5) Considering the fact that minutes of solar radiation can result in days of continuous NIR emission, how much are the external quantum efficiency (in term of out/in photons) and energy conversion efficiency (in term of out/in energy)?

These questions need to be addressed in future research. We believe that answering these questions can result in the discovery of more new efficient NIR persistent phosphors and understanding of the underlying persistent luminescence mechanisms.

REFERENCES

1 Shionoya, S. & Yen, W. M. *Phosphor Handbook*. (CRC press, 1999).

2 Hölsä, J. Persistent luminescence beats the afterglow - 400 hundred years of persistent luminescence. *Electrochemical Society Interface* **18**, 41-44 (2009).

3 Sidot, T. Sur les propriétés de la blende hexagonale. *Comptes rendus* **63**, 188-189 (1866).

4 Matsuzawa, T., Aoki, Y., Takeuchi, N. & Murayama, Y. New long phosphorescent phosphor with high brightness, $SrAl_2O_4:Eu^{2+},Dy^{3+}$. *Journal of Electrochemical Society* **143**, 2670-2673 (1996).

5 Born, M. & Wolf, E. *Electromagnetic Theory of Propagation, Interface and Diffraction of Light, 2nd ed* (Cambridge University Press, 2003).

6 Frangioni, J. V. *In vivo* near-infrared fluorescence imaging. *Current Opinion in Chemical Biology* **7**, 626-634 (2003).

7 Zhang, J., Zhang, Z., Wang, T. & Hao, W. Preparation and characterization of a new long afterglow indigo phosphor $Ca_{12}Al_{14}O_{33}$:Nd,Eu. *Materials Letters* **57**, 4315-4318 (2003).

8 Jia, D. & Yen, W. M. Trapping mechanism associated with electron delocalization and tunneling of $CaAl_2O_4:Ce^{3+}$, a persistent phosphor. *Journal of Electrochemical Society* **150**, H61-H65 (2003).

9 Aitasalo, T., Hölsä, J., Jungner, H., Lastusaari, M. & Niittykoski, J. Thermoluminescence study of persistent luminescence materials: Eu^{2+}- and R^{3+}-doped calcium aluminates, $CaAl_2O_4:Eu^{2+},R^{3+}$. *Journal of Physical Chemistry B* **110**, 4589-4598 (2006).

10 Lin, Y., Tang, Z. & Zhang, Z. Preparation of long-afterglow $Sr_4Al_{14}O_{25}$-based luminescent material and its optical properties. *Materials Letters* **51**, 14-18 (2001).

11 Chang, C., Mao, D., Shen, J. & Feng, C. Preparation of long persistent $SrO \cdot 2Al_2O_3$ ceramics and their luminescent properties. *Journal of Alloys and Compounds* **348**, 224-230 (2003).

12 Jia, D., Wang, X. J., van der Kolk, E. & Yen, W. M. Site dependent thermoluminescence of long persistent phosphorescence of $BaAl_2O_4:Ce^{3+}$. *Optics Communications* **204**, 247-251 (2002).

13 Kodama, N., Takahashi, T., Yamaga, M., Tanii, Y., Qiu, J. & Hirao, K. Long-lasting phosphorescence in Ce^{3+}-doped $Ca_2Al_2SiO_7$ and $CaYAl_3O_7$ crystals. *Applied Physics Letters* **75**, 1715-1717 (1999).

14 Jiang, L., Chang, C. & Mao, D. Luminescent properties of $CaMgSi_2O_6$ and $Ca_2MgSi_2O_7$ phosphors activated by Eu^{2+}, $Dy^{3+}$and Nd^{3+}. *Journal of Alloys and Compounds* **360**, 193-197 (2003).

15 Jiang, L., Chang, C., Mao, D. & Zhang, B. A new long persistent blue-emitting $Sr_2ZnSi_2O_7:Eu^{2+}$, Dy^{3+} prepared by sol-gel method. *Materials Letters* **58**, 1825-1829 (2004).

16 Lin, Y., Tang, Z., Zhang, Z. & Nan, C. W. Luminescence of Eu^{2+} and Dy^{3+} activated $R_3MgSi_2O_8$-based (R=Ca, Sr, Ba) phosphors. *Journal of Alloys and Compounds* **348**, 76-79 (2003).

17 Kodama, N., Tanii, Y. & Yamaga, M. Optical properties of long-lasting phosphorescent crystals Ce^{3+}-doped $Ca_2Al_2SiO_7$ and $CaYAl_3O_7$. *Journal of Luminescence* **87-89**, 1076-1078 (2000).

18 Wang, Y., Wang, Z., Zhang, P., Hong, Z., Fan, X. & Qian, G. Preparation of Eu^{2+} and Dy^{3+} co-activated $CaAl_2Si_2O_8$-based phosphor and its optical properties. *Materials Letters* **58**, 3308-3311 (2004).

19 Jia, D., Zhu, J. & Wu, B. Trapping Centers in $CaS:Bi^{3+}$ and $CaS:Eu^{2+},Tm^{3+}$. *Journal of the Electrochemical Society* **147**, 386-389 (2000).

20 Pang, R., Li, C., Zhang, S. & Su, Q. Luminescent properties of a new blue long-lasting phosphor $Ca_2P_2O_7:Eu^{2+}, Y^{3+}$. *Materials Chemistry and Physics* **113**, 215-218 (2009).

21 Pang, R., Li, C., Shi, L. & Su, Q. A novel blue-emitting long-lasting proyphosphate phosphor $Sr_2P_2O_7:Eu^{2+},Y^{3+}$. *Journal of Physics and Chemistry of Solids* **70**, 303-306 (2009).

22 Liu, L., Li, C., Wang, S. & Su, Q. Redshift phenomenon of the excitation light of long life emission phosphor. *Applied Physics Letters* **88**, 241107 (2006).

23 Lin, Y., Nan, C. W., Zhou, X., Wu, J., Wang, H., Chen, D. & Xu, S. Preparation and characterization of long afterglow $M_2MgSi_2O_7$-based (M: Ca, Sr, Ba) photoluminescent phosphors. *Materials Chemistry and Physics* **82**, 860-863 (2003).

24 Sakai, R., Katsumata, T., Komuro, S. & Morikawa, T. Effect of composition on the phosphorescence from $BaAl_2O_4$: Eu^{2+}, Dy^{3+} crystals. *Journal of Luminescence* **85**, 149-154 (1999).

25 Jia, D. & Yen, W. M. Enhanced V_K^{3+} center afterglow in $MgAl_2O_4$ by doping with Ce^{3+}. *Journal of Luminescence* **101**, 115-121 (2003).

26 Jia, D., Wang, X. J. & Yen, W. M. Electron traps in Tb^{3+}-doped $CaAl_2O_4$. *Chemical Physics Letters* **363**, 241-244 (2002).

27 Jia, D., Wang, X. J., Jia, W. & Yen, W. M. Persistent energy transfer in $CaAl_2O_4:Tb^{3+}$, Ce^{3+}. *Journal of Applied Physics* **93**, 148-152 (2003).

28 Nakagawa, H., Ebisu, K., Zhang, M. & Kitaura, M. Luminescence properties and afterglow in spinel crystals doped with trivalent Tb ions. *Journal of Luminescence* **102-103**, 590-596 (2003).

29 Uheda, K., Maruyama, T., Takizawa, H. & Endo, T. Synthesis and long-period phosphorescence of $ZnGa_2O_4:Mn^{2+}$ spinel. *Journal of Alloys and Compounds* **262-263**, 60-64 (1997).

30 Trojan-Piegza, J., Niittykoski, J., Hölsä, J. & Zych, E. Thermoluminescence and kinetics of persistent luminescence of vacuum-sintered Tb^{3+}-doped and Tb^{3+},Ca^{2+}-Codoped Lu_2O_3 Materials. *Chemistry of Materials* **20**, 2252-2261 (2008).

31 Hoogenstraaten, W. & Klasens, H. A. Some properties of zinc sulfide activated with copper and aobalt. *Journal of the Electrochemical Society* **100**, 366-375 (1953).

32 Wang, X. J., Jia, D. & Yen, W. M. Mn^{2+} activated green, yellow, and red long persistent phosphors. *Journal of Luminescence* **102-103**, 34-37 (2003).

33 Guo, C., Zhang, C., Lü, Y., Tang, Q. & Su, Q. Luminescent properties of Eu^{2+} and Ho^{3+} co-doped $CaGa_2S_4$ phosphor. *physica status solidi (a)* **201**, 1588-1593 (2004).

34 Lei, B., Liu, Y., Tang, G., Ye, Z. & Shi, C. A new orange-red long lasting phosphor material $Y_2O_2S:Sm^{3+}$. *Chemical Journal of Chinese University* **24**, 782 (2003).

35 Miyamoto, Y., Kato, H., Honna, Y., Yamamoto, H. & Ohmi, K. An Orange-Emitting, Long-Persistent Phosphor, $Ca_2Si_5N_8:Eu^{2+}$,Tm^{3+}. *Journal of the Electrochemical Society* **156**, J235-J241 (2009).

36 Lei, B., Liu, Y., Ye, Z. & Shi, C. Luminescence properties of $CdSiO_3:Mn^{2+}$ phosphor. *Journal of Luminescence* **109**, 215-219 (2004).

37 Fu, J. Orange and Red Emitting Long-Lasting Phosphors $MO:Eu^{3+}$(M=Ca, Sr, Ba). *Electrochemical and Solid-State Letters* **3**, 350-351 (2000).

38 Wang, X., Zhang, Z., Tang, Z. & Lin, Y. Characterization and properties of a red and orange Y_2O_2S-based long afterglow phosphor. *Materials Chemistry and Physics* **80**, 1-5 (2003).

39 Lei, B., Liu, Y., Tang, G., Ye, Z. & Shi, C. Spectra and long-lasting properties of Sm^{3+}-doped yttrium oxysulfide phosphor. *Materials Chemistry and Physics* **87**, 227-232 (2004).

40 Fang, M., Wang, H., Tan, X., Cheng, B., Zhang, L. & Xiao, Z. One-dimensional hollow SrS nanostructure with red long-lasting phosphorescence. *Journal of Alloys and Compounds* **457**, 413-416 (2008).

41 Iwasaki, M., Kim, D. N., Tanaka, K., Murata, T. & Morinaga, K. Red phosphorescence properties of Mn ions in MgO-GeO_2 compounds. *Science and Technology of Advanced Materials* **4**, 137-142 (2003).

42 Lin, Y., Nan, C.W., Cai, N., Zhou, X., Wang, H. & Chen, D. Anomalous afterglow from Y_2O_3-based phosphor. *Journal of Alloys and Compounds* **361**, 92-95 (2003).

43 Mao, S., Liu, Q., Gu, M., Mao, D. & Chang, C. Long lasting phosphorescence of Gd_2O_2S:Eu,Ti,Mg nanorods via a hydrothermal routine. *Journal of Alloys and Compounds* **465**, 367-374 (2008).

44 Jia, D., Jia, W., Evans, D. R., Dennis, W. M., Liu, H., Zhu, J. & Yen, W. M. Trapping processes in $CaS:Eu^{2+},Tm^{3+}$. *Journal of Applied Physics* **88**, 3402-3407 (2000).

45 Wang, J., Wang, S. & Su, Q. The role of excess Zn^{2+} ions in improvement of red long lasting phosphorescence (LLP) performance of beta-$Zn_3(PO_4)_2$:Mn phosphor. *Journal of Solid State Chemistry* **177**, 895-900 (2004).

46 Boutinaud, P., Sarakha, L., Cavalli, E., Bettinelli, M., Dorenbos, P. & Mahiou, R. About red afterglow in Pr^{3+} doped titanate perovskites. *Journal of Physics D-Applied Physics* **42** (2009).

47 Lian, S. X., Qi, Y., Rong, C. Y., Yu, L. P., Zhu, A. L., Yin, D. L. & Liu, S. B. Effectively leveraging solar energy through persistent dual red phosphorescence: preparation, characterization, and density functional theory study of $Ca_2Zn_4Ti_{16}O_{38}$:Pr^{3+}. *Journal of Physical Chemistry C* **114**, 7196-7204 (2010).

48 de Chermont, Q. L., Chaneac, C., Seguin, J., Pelle, F., Maitrejean, S., Jolivet, J. P., Gourier, D., Bessodes, M. & Scherman, D. Nanoprobes with near-infrared persistent luminescence for *in vivo* imaging. *Proceedings of the National Academy of Sciences of the United States of America* **104**, 9266-9271 (2007).

49 Borek, C., Hanson, K., Djurovich, P., Thompson, M., Aznavour, K., Bau, R., Sun, Y., Forrest, S., Brooks, J., Michalski, L. & Brown, J. Highly efficient, near-infrared electrophosphorescence from a Pt-metalloporphyrin complex. *Angewandte Chemie International Edition* **46**, 1109-1112 (2007).

50 Yu, N. Y., Liu, F., Li, X. F. & Pan, Z. W. Near infrared long-persistent phosphorescence in $SrAl_2O_4$:Eu^{2+}, Dy^{3+}, Er^{3+} phosphors based on persistent energy transfer. *Applied Physics Letters* **95**, 231110 (2009).

51 Yan, W. Z., Liu, F., Lu, Y. Y., Wang, X. J., Yin, M. & Pan, Z. W. Near infrared long-persistent phosphorescence in $La_3Ga_5GeO_{14}$:Cr^{3+} phosphor. *Optics Express* **18**, 20215-20221 (2010).

52 Jia, D., Lewis, L. A. & Wang, X. J. Cr^{3+}-doped lanthanum gallogermanatephosphors with long persistent IR emission. *Electrochemical and Solid State Letters* **13**, J32-J34 (2010).

53 Blasse, G. & Grabmaier, B. C. *Luminescent Materials*. (Springer-Verlag, 1994).

54 Struve, B. & Huber, G. The effect of the crystal field strength on the optical spectra of Cr^{3+} in gallium garnet laser crystals. *Applied Physics B: Lasers and Optics* **36**, 195-201 (1985).

55 Szymczak, H., M, Wardzynska. & I, E. Mylnikova. Optical spectrum of Cr^{3+} in the spinel $LiGa_5O_8$. *Journal of Physics C: Solid State Physics* **8**, 3937-3943 (1975).

56 Macfarlane, P. I., Han, T. P. J., Henderson, B. & Kaminskii, A. A. *Optical Materials* **3**, 15-24 (1994).

57 Kaminskii, A. A., Shkadarevich, A. P., Mill, B. V., Koptev, V. G., Butashin, A. V. & Demidovich, A. A. Tunable stimulated-emission of Cr^{3+} ions and generation frequency self-multiplication effect in acentric crystals of Ca-gallogermante structure. *Inorganic Materials* **24***,* 579 (1988).

58 Walsh, C. G., Donegan, J. F., Glynn, T. J., Morgan, G. P., Imbusch, G. F. & Remeika, J. P. Luminescence from beta-Ga_2O_3: Cr^{3+}. *Journal of Luminescence* **40-41**, 103-104 (1988).

59 Jose Solé, L. B. & Daniel Jaque. *An Introduction to the Optical Spectroscopy of Inorganic Solids* (John Wiley & Sons, 2005).

60 Tanabe, Y. & Sugano, S. On the absorption spectra of complex ions. I. *Journal of the Physical Society of Japan* **9**, 753-766 (1954).

61 Tanabe, Y. & Sugano, S. On the absorption spectra of complex ions II. *Journal of the Physical Society of Japan* **9**, 766-779 (1954).

62 Tanabe, Y. & Sugano, S. On the absorption spectra of complex ions, III The calculation of the crystalline field strength. *Journal of the Physical Society of Japan* **11**, 864-877 (1956).

63 Aitasalo, T., Hölsä, J., Jungner, H., Krupa, J. C., Lastusaari, M., Legendziewicz, J. & Niittykoski, J. Effect of temperature on the luminescence processes of $SrAl_2O_4:Eu^{2+}$. *Radiation Measurements* **38**, 727-730.

64 McKeever, S. W. S. *Thermoluminescence of Solids*. (Cambridge University Press, 1985).

65 Yamaga, M., Ohsumi, Y., Nakayama, T., Kashiwagura, N., Kodama, N. & Han, T. Long-lasting phosphorescence in Ce-doped oxides. *Journal of Materials Science: Materials in Electronics* **20**, 471-475 (2009).

66 Dorenbos, P. Mechanism of persistent luminescence in Eu^{2+} and Dy^{3+} codoped aluminate and silicate compounds. *Journal of the Electrochemical Society* **152**, H107-H110 (2005).

67 Kostyk, L., Luchechko, A., Zakharko, Y., Tsvetkova, O. & Kuklinski, B. Cr-related centers in $Gd_3Ga_5O_{12}$ polycrystals. *Journal of Luminescence* **129**, 312-316 (2009).

68 Jablonski, A. Efficiency of anti-stokes fluorescence in dyes. *Nature* **131**, 839-840 (1933).

69 Randall, J. T. & Wilkins, M. H. F. Phosphorescence and electron traps. I. The study of trap distributions. *Proceedings of Royal Society A* **184**, 365-389 (1945).

70 Garlick, G. F. J. & Gibson, A. F. The electron trap mechanism of luminescence in sulphide and silicate phosphors. *Proceedings of the Physical Society* **60**, 574-590 (1948).

71 May, C. E. & Partridge, J. A. Thermoluminescent kinetics of alpha-irradiated alkali halides. *Journal of Chemical Physics* **40**, 1401-1409 (1964).

72 Quan, Y., Fang, D., Zhang, X. Y., Liu, S. Q. & Huang, K. L. Synthesis and characterization of gallium oxide nanowires via a hydrothermal method. *Materials Chemistry and Physics* **121**, 142-146 (2010).

73 Kuo, C. L. & Huang, M. H. The growth of ultralong and highly blue luminescent gallium oxide nanowires and nanobelts, and direct horizontal nanowire growth on substrates. *Nanotechnology* **19**, 155604 (2008).

74 Binet, L. & Gourier, D. Origin of the blue luminescence of β-Ga_2O_3. *Journal of Physics and Chemistry of Solids* **59**, 1241-1249 (1998).

75 Nogales, E., Garcia, J. A., Mendez, B. & Piqueras, J. Doped gallium oxide nanowires with waveguiding behavior. *Applied Physics Letters* **91**, 133108 (2007).

76 Vanithakumari, S. C. & Nanda, K. K. A One-step method for the growth of Ga_2O_3-nanorod-based white-light-emitting phosphors. *Advanced Materials* **21**, 3581-3584 (2009).

77 Dai, Z. R., Pan, Z. W. & Wang, Z. L. Gallium oxide nanoribbons and nanosheets. *Journal of Physical Chemistry B* **106**, 902-904 (2002).

78 Li, G. G., Peng, C., Li, C. X., Yang, P. P., Hou, Z. Y., Fan, Y., Cheng, Z. Y. & Lin, J. Shape-controllable synthesis and morphology-dependent luminescence properties of GaOOH:Dy^{3+} and β-Ga_2O_3:Dy^{3+}. *Inorganic Chemistry* 49**, 1449-1457 (2010).**

79 Gu, Z., Zhai, T., Gao, B., Sheng, X., Wang, Y., Fu, H., Ma, Y. & Yao, J. Controllable assembly of WO_3 nanorods/nanowires into hierarchical nanostructures. *Journal of Physical Chemistry B* **110**, 23829-23836 (2006).

80 Nogales, E., Garcia, J. A., Mendez, B. & Piqueras, J. Red luminescence of Cr in β-Ga_2O_3 nanowires. *Journal of Applied Physics* **101**, 033517 (2007).

81 Yeom, T. H., Kim, I. G., Lee, S. H., Choh, S. H. & Yu, Y. M. Electron paramagnetic resonance characterization of Cr^{3+} impurities in a beta-Ga_2O_3 single crystal. *Journal of Applied Physics* **93**, 3315-3319 (2003).

82 Grinberg, M., Barzowska, J., Shen, Y. R. & Bray, K. L. Inhomogeneous broadening of Cr^{3+} luminescence in doped $LiTaO_3$. *Physical Review B* **63**, 214104 (2001).

83 Grinberg, M., Macfarlane, P. I., Henderson, B. & Holliday, K. Inhomogeneous broadening of optical transitions dominated by low-symmetry crystal-field components in Cr^{3+}-doped gallogermanates. *Physical Review B* **52**, 3917-3929 (1995).

84 Yamaga, M., Macfarlane, P. I., Henserson, B., Holliday, K., Takeuchi, H., Yosida, T. & Fukui, M. Substitutional disorder and the ground state spectroscopy of gallogermanate crystals. *Journal of Physics: Condensed Matter* **9**, 569-578 (1997).

85 Macfarlane, P. I., Henserson, B., Holliday, K. & Grinberg, M. Substitutional disorder and the optical spectroscopy of gallogermanate crystals. *Journal of Physics: Condensed Matter* **8(21)**, 3933-3946 (1996).

86 Champagnon, B. & Pilla, O. Comment Comparison of the fluorescence lifetimes of Cr^{3+} in crystals, glasses and glass ceramics and their use to interpret the effect of pressure on ruby. *Chemical Physics Letters* **161**, 90-91 (1989).

87 Garapon, C., Manaa, H. & Moncorge, R. Absorption and fluorescence properties of Cr^{3+} doped nonstoichiometric green spinel. *Journal of Chemical Physics* **95**, 5501-5512 (1991).

88 Henderson, B. & Imbush, G. F. *Optical Spectroscopy of Inorganic Solids*. (Oxford University Press, 1989).

89 Yamaga, M., Masui, Y. & Sakuta, S. Radiative and nonradiative decay processes responsible for long-lasting phosphorescence of Eu^{2+}-doped barium silicates. *Physical Review B* **71**, 205102 (2005).